INTERNATIONAL JOURNAL OF CLIMATOLOGY
Int. J. Climatol. (2017)
Published online in Wiley Online Library
(wileyonlinelibrary.com) DOI: 10.1002/joc.5004

RMetS
Royal Meteorological Society

Satellite-retrieved direct radiative forcing of aerosols over North-East India and adjoining areas: climatology and impact assessment

Jhuma Biswas,[a,b]* Binita Pathak,[a] Falguni Patadia,[c,d] Pradip K. Bhuyan,[a] Mukunda M. Gogoi[e] and S. Suresh Babu[e]

[a] *Centre for Atmospheric Studies, Dibrugarh University, Assam, India*
[b] *Department of Physics, Birjhora Mahavidyalaya, Bongaigaon, Assam, India*
[c] *Climate and Radiation Laboratory, NASA Goddard Space Flight Center, Greenbelt, MD, USA*
[d] *Goddard Earth Sciences Technology and Research (GESTAR), Morgan State University (MSU), Baltimore, MD, USA*
[e] *Space Physics Laboratory, Vikram Sarabhai Space Centre, Thiruvananthapuram, Kerala, India*

ABSTRACT: In order to understand the climatic implications of atmospheric aerosols, top of atmosphere (TOA) shortwave (SW, 0.3–5 µm) fluxes and aerosol optical depth (AOD) at 550 nm retrieved simultaneously by clouds and the earth's radiant energy system (CERES) and moderate resolution imaging spectroradiometer (MODIS) instruments, respectively, are analysed over North-East India and its adjoining areas for the period July 2002–December 2013. The aerosol-free TOA flux obtained by establishing the linear regression between CERES SW TOA fluxes and MODIS AODs exhibits strong seasonality with peak values in monsoon and minimum in winter. Same seasonality is captured by the Santa Barbara DISORT Atmospheric Radiative Transfer (SBDART) model, but with difference in absolute values. SBDART code is used to extend instantaneous radiative forcing estimates into 24-h averages. AOD over the North East India region with complex terrain shows altitudinal variation with maximum value at the lowest elevation site Dhaka and minimum value at the high-altitude locations Shillong and Aizwal. In general, strong seasonality in AOD is observed with a peak in pre-monsoon (March–May) and dip in post-monsoon (October–November) at all the locations. The direct instantaneous TOA shortwave aerosol radiative forcing (SWARF) shows maximum values in pre-monsoon over all the locations except at Guwahati, Banmauk, Aizawl, and Shillong. The lowest value of instantaneous SWARF is observed in post-monsoon except at Banmauk and Shillong. Climatologically TOA diurnally averaged SWARF varies between $-6.95\,\mathrm{W\,m^{-2}}$ in Aizawl to $-20.39\,\mathrm{W\,m^{-2}}$ in Shillong. In general, the TOA SW forcing efficiency is highest in monsoon at all the locations. The radiative forcing efficiency is found to be less negative when surface reflectance increases.

KEY WORDS aerosol optical depth; aerosol radiative forcing; CERES; regional air quality; remote sensing

Received 13 June 2016; Revised 22 December 2016; Accepted 30 December 2016

1. Introduction

Aerosol radiative forcing (ARF) is a concept used for the quantitative comparison of the strength of different natural and anthropogenic agents causing Earth's climate change. For the thermodynamical equilibrium in Earth–atmosphere system, which maintains the temperature of the Earth, a global energy balance must exist between energy coming from the Sun and energy returned to space from the Earth–atmosphere system (Wielicki *et al.*, 1996; Hansen *et al.*, 1997). Climatic effect of aerosols is usually quantified in terms of radiative forcing, defined as the effect of atmospheric aerosols on the radiative fluxes at the top of the atmosphere as well as at the surface of the Earth due to the absorption of solar radiation within the atmosphere. Thus, ARF is a measure of perturbations caused by the atmospheric species in Earth's overall radiation budget. ARF at the top of the atmosphere is defined as the difference between the outgoing shortwave (SW) solar flux without and with aerosols present in the atmosphere. According to Intergovernmental Panel on Climate Change (IPCC), currently the radiative effect of aerosols is one of the most active research areas in climate studies (IPCC, 2007). Most of the aerosols (e.g. sea salt particles, sulphates, nitrates, organic carbons, etc.) directly reflect sunlight back into space, thereby enhancing planetary albedo (reflectance) and leading to a negative surface forcing but the presence of absorbing aerosols such as black carbon (BC) can change the sign of forcing from negative (cooling) to positive (heating) by absorbing the SW radiation. Whether atmospheric aerosols exert a net cooling or a net heating effect will depend on the type of aerosol particles and the albedo of the underlying surface (Keil and Haywood, 2003). Biomass burning aerosols make a significant, but weak, quantified contribution to the anthropogenic radiative forcing of climate (IPCC, 2007)

---

* Correspondence to: J. Biswas, Centre for Atmospheric Studies, Dibrugarh University, Jyoti Baatsara, Dibrugarh, Assam 786004, India. E-mail: jhumabiswasdu@gmail.com

and may affect the local atmospheric circulation pattern (Ramanathan and Carmichael, 2008). The spatial heterogeneity in aerosols distribution throughout the globe results in either positive or negative forcing at TOA, which finally affects the global average TOA forcing and thus the global climate system. Aerosols are inhomogeneously distributed over the globe and their radiative forcing is strongly dependent on underlying surface characteristics or in other words the geographical location on the Earth (Meywerk and Ramanathan, 1999). Natural and man-made changes in the atmosphere, land, ocean, biosphere, and cryosphere can perturb the Earth's radiation budget and thus affects the Earth's climate producing radiative forcing (IPCC, 2013). Scientific understanding of the aerosol radiative effects from regional to global scales is still uncertain, particularly in locations with complex emission sources and land ecosystems (IPCC, 2007; Reid *et al.,* 2013). The quantitative estimation of ARF is more complex than the radiative forcing estimation of greenhouse gases due to the large spatiotemporal variability of aerosol particles along with their much shorter atmospheric lifetime compared with the lifetime of significant greenhouse gases (Panicker and Lee, 2012). Global monitoring of aerosols from space by using satellites provides a distinctive chance to study the effects of aerosols in different areas over the Earth's surface. A large number of studies on atmospheric aerosol have been performed by using Clouds and the Earth's Radiant Energy System (CERES) data over different places in the world (Satheesh and Ramanathan, 2000; Li *et al.,* 2000; Rajeev and Ramanathan, 2001; Christopher and Zhang, 2002a, 2002b; Loeb and Kato, 2002; Zhang and Christopher, 2003; Zhang *et al.,* 2005; Christopher *et al.,* 2006; Gupta *et al.,* 2008; Patadia *et al.,* 2008b; Yan *et al.,* 2011; Corbett *et al.,* 2012; Sena *et al.,* 2013; Feng and Christopher, 2013; Feng and Christopher, 2014; Sena and Artaxo, 2015; Sundström *et al.,* 2015 etc.). The majority of the studies were conducted generally over either oceanic, deserts or land region. Patadia *et al.* (2008a) used instantaneous SW flux and aerosol optical depth (AOD) at 558 nm retrieved by CERES and multi-angle imaging spectroradiometer (MISR) instruments respectively on-board Terra satellite to estimate the top of atmosphere (TOA) direct shortwave aerosol radiative forcing (SWARF) over the Amazon Basin for the period 2000–2005. Feng and Christopher (2013) used CERES, moderate resolution imaging spectroradiometer (MODIS) and MISR data sets from NASA's Terra satellite to provide a quantitative evaluation of regional cloud-free diurnally averaged TOA SW aerosol radiative effects over both land and ocean during December, 2006–November, 2007. Pathak *et al.* (2010) have reported ARF over Dibrugarh, a remote continental location in North-East India on the basis of ground-based observations. But such report from a single location is insufficient to characterize the total aerosol environment for the whole region. Extensive characterization of aerosols and their effect is still lacking in North-East India and adjoining region. As such the present study conducted to characterize the aerosols and their climatic impact may provide the background information on the aerosol environment in the complex terrain of North-East India. The North-East India, due to less industrialization and low population density, is expected to contain minimum aerosols in the atmosphere, but at the same time, its unique topography acts as a sink for the transported aerosols which may sustain in the atmosphere for long time. Again as the region may be considered as an extension of the Indo-Gangetic plains (IGP) (Pathak *et al.,* 2014), surrounded by mountains and open only towards the west which provides a normal entryway for transportation of aerosols through the western corridor (Gogoi *et al.,* 2009, 2011), Pathak *et al.* (2010, 2013). The complex nature of atmospheric aerosols and their radiative effects over a region make it complicated to model their effects with high confidence. Climate change, whether driven by natural or anthropogenic forcing, can cause changes in the likelihood of the occurrence or power of significant weather and climate events or both (IPCC, 2013). It is, therefore, very important to study the effects (direct as well as indirect) of aerosols over different locations because of its important role in Earth's climate.

The main goal of the present study is to assess the spatiotemporal distributions of SWARF at the TOA and aerosol forcing efficiency over different locations in North-East India and adjoining areas for the last deacde, July 2002–December 2013. This work is mainly based on CERES TOA SW radiative flux and MODIS AOD (τ) data sets from NASA's Aqua satellite. Even though a lot of research has been carried out over the IGP but not much has been done over the present region of interest. Thus this work will fill the knowledge gap in the country. In order to assess the accuracy of the MODIS-derived AOD, intercomparison has been done between the MODIS AOD with the ground-based observations for locations where measurements are available. Furthermore, we have compared the CERES Aqua instantaneous SW flux with the Santa Barbara DISORT Atmospheric Radiative Transfer (SBDART) model derived instantaneous SW flux.

1.1. Study region

For the present study, nine different locations have been selected in North-East India and adjoining areas with increasing altitude: Dhaka (DAC), Agartala (AGA), Dhubri (DHB), Guwahati (GHY), Dibrugarh (DBR), Banmauk (BNK), Imphal (IPH), Aizawl (AZL) and Shillong (SHN) (Figure 1, where the colour bar represents altitude). The region of North-East India is surrounded by Bhutan and China in the north, Myanmar in the south and southeast and Bangladesh in the west. The North-East India, which represents a transition between South and Southeast Asia, is the easternmost region of India consisting of seven states: Arunachal Pradesh, Assam, Manipur, Meghalaya, Mizoram, Nagaland and Tripura plus the Himalayan state of Sikkim covering an area of 255 168 km^2 where nearly 64% of the total geographical area is covered by forest. The height of the region varies from 50 m above mean sea level (AMSL) in the lower Brahmaputra region to higher height of 7000 m AMSL of Himalaya. Rocky

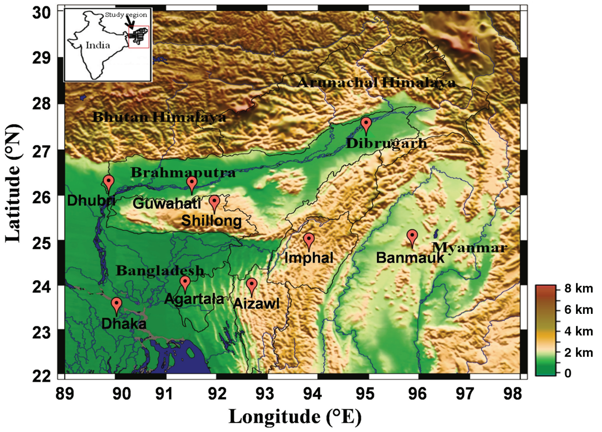

Figure 1. Map of North-East India and adjoining areas showing the topography. The red symbols indicate the observation locations. Inset map shows the map of India with study region marked within the red box. Colour bar indicates altitude.

surface, alpine vegetation, and snow-capped high peaks dominate the physical landscape of this region where 72% area is under hilly ecosystem. The region receives the highest rainfall every year during June–August and this has made the region to be clothed with diverse and dense vegetation. Biomass burning, especially as a part of shifting cultivation (slash and burn cultivation), locally known as Jhuming, involving burning of stretches of forests and growing a number of crops after every 4 or 5 years, is widely prevalent in this region and it, along with brick kilns (coal-fired) and oil and gas fields makes this region a strong source of anthropogenic emissions. Kharol *et al.* (2008) reported that the natural jhum cycle, used to be 5–6 years earlier, has reduced to 2–3 years due to rising population leading to the change of primary forests to secondary forests and deciduous systems with a subsequent loss of biodiversity.

Dhaka (23.4°N, 90.2°E, 4 m AMSL), tenth largest city in the world is the capital city of Bangladesh. It is one of the densely populated megacities in the world, with about 15 million inhabitants within a 300-km^2 area (Salman *et al.,* 2008) and population density being 19 447 km^{-2}. Agartala (23.9°N, 91.2°E, 15 m AMSL), the capital of the Indian state of Tripura bordering Bangladesh is the second largest city in North-East India after Guwahati, both in municipal area and population with population density 5730 km^{-2}. Dhubri (26°N, 90°E, 28 m AMSL), the district headquarter of the second most populous districts of western Assam, is in the pathway of winds from the western India and beyond. It is an old town situated on the bank of the Brahmaputra and Gadadhar rivers and is known as the 'Land of Rivers' as it is covered three sides by rivers. Guwahati (26.2°N, 91.7°E, 55 m AMSL), an ancient urban area of Assam is the largest city in North-East India. It is a major metropolis of eastern India and one of the fastest developing cities of India with population density 4460 km^{-2}. The city lies on the banks of the Brahmaputra River and the foothills of the Shillong plateau. It is the Gateway of North Eastern Region of India and a principal centre of sociocultural, industrial, trade and commerce of the region. Dibrugarh (27.3°N, 94.6°E, 111 m AMSL) in the upper Brahmaputra Basin is the major commercial centre of oil and tea industry, communication and health care of the state of Assam with a population density of 393 km^{-2}. Banmauk (24.4°N, 95.8°E, 279 m AMSL) is a township in Katha district in the Sagaing region of north-central Myanmar with population density 33 km^{-2}. Imphal (24.8°N, 93.9°E, 786 m AMSL), is the capital city of Manipur with a population density of 640 km^{-2}. Aizawl (23.7°N, 92.7°E, 1001m AMSL), is the scenic capital city of Mizoram, located north of the Tropic of Cancer in the northern part of Mizoram where the population density is 234 km^{-2}. Over Mizoram, the average annual rainfall is 2150 mm which occurs generally between the month of June and September during the southwest monsoon and 75.6% area is covered by forest (Sati and Rinawma, 2014). Shillong (25.6°N, 91.9°E, 1496 m AMSL), the capital city of Meghalaya with a population density of 234 km^{-2} is just 55 km from Mawsynram, the world's wettest place. Shillong receives heavy rainfall during monsoon and the rainy season usually lasts longer than rest of India.

North-East India is one of the 18 largest biodiversities in the world. Large vegetation in the North-East region is a good source of volatile organic compounds (VOCs) along with biological aerosols. The region is also rich in soil organic carbon. Biomass burning associated with the shifting cultivation practice releases a huge amount of BC and trace gases, which peaks in the month of March–April (Pathak *et al.,* 2013). An open coal mining, brick kilns, oil and gas fields contribute to carbonaceous aerosols and gases. Earlier researchers (Gogoi *et al.,* 2009, 2011; Pathak *et al.,* 2012) from Dibrugarh, the easternmost location in North-East India have shown how transportation from IGP, mainland and western India and western Asia intensifies the aerosol loading in the region, particularly during pre-monsoon (PM, March–May) season. The region exhibits typical subtropical weather pattern with mild, cool, dry and relatively short winter (W, December–February), hot and humid pre-monsoon and extended rainy seasons of monsoon (M, June–September) and post-monsoon or retreating monsoon (RM, October–November).

2. Data and methodology

CERES instrument is one of the highest priority scientific satellite instruments on the Earth Observing System of NASA's space-borne measurement programme and provides global observations of solar reflected radiation as well as Earth's emitted thermal radiation. It was first flown aboard the TRMM spacecraft whose 35° inclination orbit permitted for radiation budget data collection over all local times, i.e. all solar zenith angles for the latitude range (Smith *et al.,* 2004). It has the TOA SW channel for measuring reflected sunlight (0.3–5 μm), an infrared (IR) channel (8–12 μm) for measuring Earth-emitted thermal radiation 'window' region and a total channel (0.3–200 μm) for total radiation measurement (Wielicki *et al.,* 1996). The well-calibrated TOA radiance measurements with a spatial resolution of 20 km × 20 km are converted to reflected and emitted fluxes with the help of angular distribution models (Loeb *et al.,* 2003, 2005).

Presently, there are four CERES instruments working on two satellites (Terra and Aqua) which are based on the successful Earth Radiation Budget Experiment scanning radiometer. CERES instruments on board the Terra and Aqua satellites have been operating since December 1999 and May 2002, respectively. Another CERES instrument is on board the Suomi-National Polar-Orbiting Partnership (SNPP) mission launched in October 2011. CERES operates in three scanning modes: across the satellite ground track (cross-track), along the direction of the satellite ground track (along-track) and in a Rotating Azimuth Plane. Aerosols together with cloud properties are inferred from the MODIS imager, along with CERES on board Aqua spacecraft. MODIS is a 36-channel; 1-km, 500-m, and 250-m nadir resolution; narrow and scanner operating in a cross-track mode. This CERES Single Scanner Footprint (SSF) product contains MODIS (MOD04) aerosol and cloud properties for each CERES footprint (20 km at nadir) in addition to the SW and longwave fluxes (Remer *et al.,* 2005). We use MODIS's AOD contained in CERES-SSF product due to MODIS's larger swath width and consequently higher spatial coverage. By using point spread functions, MODIS aerosol data which are originally obtainable at 10-km spatial resolution is translated into CERES 20-km resolution (Smith, 1994).

In this study, we have used CERES−SSF product having concurrent information of SW fluxes and AODs in it. MODIS AOD data will refer to information within the CERES−SSF file. Since CERES is a broadband instrument, it is suitable to study the TOA radiative effects of aerosol in the solar part of the spectrum. The most recently available CERES_SSF_XTRK_MODIS_Edition3A level 2 data set containing merged information from MODIS imager on board Aqua were used in the present analysis. For Aqua Edition3A, the MODIS aerosols are from collection 4 before 30 April 2006 and after that date, the MODIS aerosols are from collection 5. The methodology used in this work is shown in Figure 2(a) and will be discussed in detail in the following section.

2.1. Instantaneous ARF

The instantaneous TOA SWARF in cloud-free sky conditions is defined as the difference in TOA SW fluxes from the CERES in the absence (F_{clr}) and in the presence of aerosols (F_{aero}) at the satellite overpass time (~0800 UTC) (e.g. Zhang *et al.,* 2005; Patadia *et al.,* 2008a), i.e.,

$$\mathrm{SWARF}_{\mathrm{CERES}} = F_{\mathrm{clr}} - F_{\mathrm{aero}} \tag{1}$$

Here, F_{clr}, i.e. flux with no AOD condition and is derived from the y-intercept of the regression line between all MODIS AOD and instantaneous TOA CERES SW flux for each latitude−longitude grid (Figure 2(b)). F_{aero} is the cloud-free TOA SW flux with aerosols. SWARF can be positive or negative. The negative sign of SWARF is obtained if $F_{\mathrm{aero}} > F_{\mathrm{clr},}$ which implies that aerosols produce a cooling effect, whereas $F_{\mathrm{aero}} < F_{\mathrm{clr}}$ is indicative of warming effect caused by aerosols. The linearity of the outgoing SW TOA flux with AOD does not hold for high values of AOD (Sena *et al.,* 2013), therefore, AOD > 2 were discarded in the linear fit. In low AOD conditions, the single-scattering assumption is a good approximation, but in high AOD conditions, multiple scattering from aerosols presents non-linearity in the fit. F_{clr} is computed if the number of data points within a grid is >10 and a positive correlation exists ($R > 0.2$) between SW flux and AOD. Since there is a significant increase in the pixel size at higher scan angles, only the CERES pixels with viewing and solar zenith angles less than 60 are used in the analysis (Christopher and Zhang, 2002b; Patadia *et al.,* 2008b). Using the MODIS cloud cover information (retained in the merged data sets from the CERES SSF product) cloudy pixels is first removed if the cloud fraction is greater than 0.5% for sub-pixel clear area percentages is greater than 99.9% (Patadia *et al.,* 2008b).

2.2. Diurnally averaged ARF

The SBDART model can be used to work out the radiative effects of the boundary layer and upper-level atmospheric aerosols. Using SBDART Model (Ricchiazzi *et al.,* 1998), the instantaneous flux at the time of satellite overpass ($F_{\mathrm{calc}}I$) and the daily average flux ($F_{\mathrm{calc}}24$) are calculated. The wavelength range selected for the simulations in SBDART model varies from 0.3 to 5.0 μm, corresponding to the CERES SW channel. The tropical atmospheric profile has been considered in the input of the SBDART model. For tropical atmospheric, the default values of water vapour and ozone are 4.117 $\mathrm{g\,cm^{-2}}$ and 0.253 atm-cm, respectively. To calculate the SW flux with aerosols, we have used the seasonal variation of MODIS AOD at 550 nm separately for all the locations. Based on the nature of the locations, we have considered either rural or urban aerosol type in the SBDART model. In these models wavelength dependent constant values of the asymmetry parameter, which is a function of aerosol size and single scattering albedo are adopted (Ricchiazzi *et al.,* 1998 and references therein). More details about the SBDART model has been described in Pathak *et al.* (2010, 2016).

The SWARF_{24} are calculated by weighting the instantaneous SWARF obtained from CERES−SSF data by the ratio of the daily SWARF ($F_{\mathrm{calc}}24$) over the instantaneous SWARF obtained from SBDART simulations (Remer and Kaufman, 2006). Thus, the 24-h average SWARF is obtained from the following formula,

$$\mathrm{SWARF}_{24} = \mathrm{SWARF}_{\mathrm{CERES}} \times \left(F_{\mathrm{calc}}24 \,/\, F_{\mathrm{calc}}I\right) \tag{2}$$

where $\mathrm{SWARF}_{\mathrm{CERES}}$ is the instantaneous CERES TOA SWARF, $F_{\mathrm{calc}}24$ is the model-derived daily average flux and $F_{\mathrm{calc}}I$ is the model-derived flux value at the instantaneous time of the overpass.

2.3. Instantaneous forcing efficiency

The instantaneous forcing efficiency is a key parameter for studying the climatic effects of aerosols. It

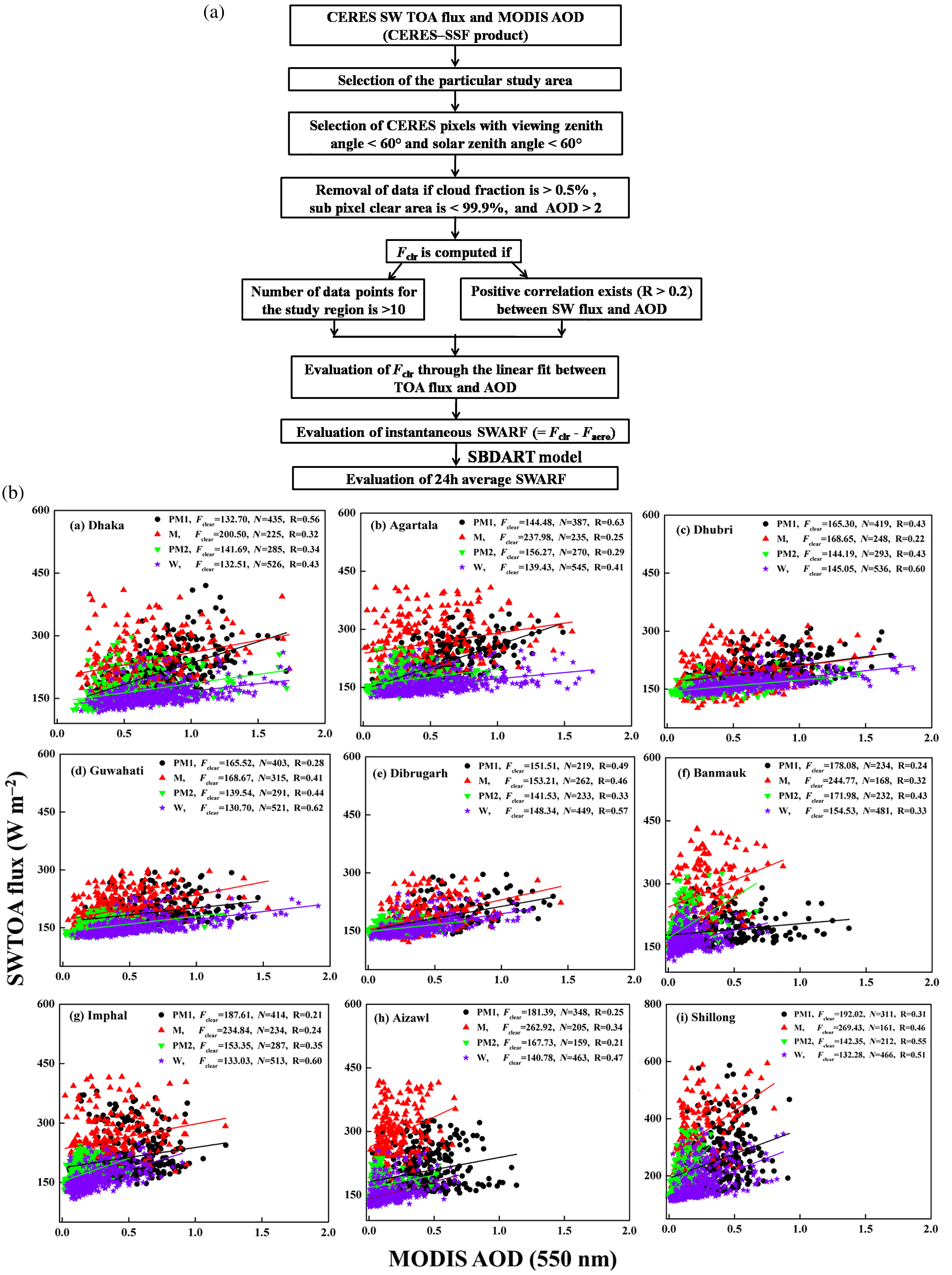

Figure 2. (a) The methodology for evaluation of SW TOA diurnal average aerosol radiative forcing from simultaneous CERES SW flux and MODIS AOD for the period July 2002–December 2013 over North-East India and adjoining areas. (b) Estimation of F_{clr} over different location in North-East India and adjoining areas for four seasons for the period July 2002–December 2013. Different coloured dots represent seasonal values (Black = MAM, Red = JJAS, Green = ON, and Blue = DJF). The linear regression line between SW TOA flux and AOD for all data points is also shown. The locations are arranged as a, b, c, etc. in increasing order of altitude.

defines the rate of change of the net irradiance per unit increase in the AOD. The regression relationship between MODIS-derived AOD at 550 nm and the instantaneous SWARF have been used to determine the TOA instantaneous ARF efficiency for different locations over North-East India and adjoining areas. The forcing efficiency was given by the slope of the best-fit line between instantaneous SWARF *versus* corresponding AOD (Ramana *et al.,* 2004). Since slopes estimated by such linear regression relations may be affected by outliers, hence to reduce these effects and to obtain stable relationships, we have used median values in generating the regressions. Surface reflectance is a significant factor in determining the strength of ARF. MODIS-derived surface reflectance data have been used to examine the variation of radiative forcing efficiency with the surface reflectance at 2.1 μm.

Uncertainties in ARF estimations using CERES satellite are because of uncertainty associated with fluxes due to calibration ($\pm 0.4\,\mathrm{W\,m^{-2}}$), unfiltering of TOA radiances ($\pm 0.4\,\mathrm{W\,m^{-2}}$), conversion of radiance to flux by Angular Distributio Models over land ($\pm 0.4\ \mathrm{W\,m^{-2}}$), cloud contamination and uncertainty in the estimation of clear-sky fluxes (Patadia *et al.,* 2008a). The uncertainty in CERES SW flux measurements at TOA is mostly due to cloud contamination, radiance-to-flux conversion and instrument calibration and the value can go up to $\sim 1\ \mathrm{W\,m^{-2}}$ for direct aerosol forcing estimation (Loeb and Kato, 2002). The highest source of uncertainty for determination of ARF is because of the uncertainty of MODIS retrieved AOD at 550 nm. Nakajima *et al.* (2007) reported that the underestimation of the radiative forcing is due to overestimation of the simulated cloudiness and aerosol scale height. On the other hand, the possible error in the simulated surface albedo may cause an overestimation of the magnitude of the radiative forcing over the land area (Nakajima *et al.,* 2007).

3. Results and discussion

3.1. Spatiotemporal distribution of AOD

Figure 3(a) shows the spatiotemporal variations of AOD at 550 nm over different locations (presented on *x*-axis in increasing order of altitude) in North-East India and its adjoining areas for the period July 2002–December 2013 (also see Figure 1 and Table 1). For all the locations, the maximum AOD is obtained in pre-monsoon whereas AOD is minimum in post-monsoon season. North-East India experiences anthropogenic biomass burning, particularly in pre-monsoon, which is a major contributor of aerosols over the study region (Pathak *et al.,* 2016 and references therein). AOD starts to build up in winter again. The decrease in AOD in monsoon is associated with cloud scavenging and wet removal processes (Pathak *et al.,* 2010).

Earlier in the North-East region, by using MODIS retrieved fire product Kalita and Bhuyan (2011) and Pathak *et al.* (2013) have reported peak fire count in March–April. Kharol *et al.* (2008) has also observed high AOD at 550 nm in North-East India due to enhanced fire activities peaking in March–April over this region. The effect of aerosols generated from biomass burning in Myanmar has been experienced over the Bay of Bengal (BoB) by Nair *et al.* (2008). Most of the present study locations being the capital cities of different states/country (except DBR and BNK) are small urban pockets. Thus, in addition to the biomass burning local urban pollutions such as emissions from brick kilns, oil/gas fields and coal mines and other anthropogenically generated aerosols from biofuels/fossil fuel emissions are major sources of aerosols in the region. Again, DAC, AGA, SHN, DHB and GHY being located at the outflow pathways of winter haze from IGP, exhibit appreciable aerosol loading in winter. The prevailing westerly winds, combined with the orography of the region confine the aerosols transported from western locations, including IGP haze, into a rather narrow channel in the North-East Indian region. Thus, the region acts as a sink to the aerosols, where these can sustain for a long time until removed from the atmosphere and contributes to appreciable loading. Trajectory analysis carried out over the region identifies IGP, west and mainland India, west Asia, and BoB, the Arabian Sea as most potential source regions contributing to the aerosol loading over the region in different seasons (figure not shown). Thus, external influences significantly determine the aerosol environment in the region, which has also been reported by several earlier researchers like Gogoi *et al.* (2009, 2011) and Pathak *et al.* (2012, 2016) etc. Kumar (2013) has reported same seasonality in AOD obtained from MODIS Terra satellite, over eight major cities of North-East India (Itanagar, Gangtok, Guwahati, Kohima, Imphal, Aizawl, Agartala, and Shillong) for the period of 2001–2010. Again, a similar seasonal variations of AOD over DBR and DAC has been reported earlier by Pathak *et al.* (2010) and Mamun *et al.* (2014), respectively.

From Figure 3(a) it is evident that the regional AOD shows a strong gradient which generally decreases with increase in altitude for all the season and vice versa. Dumka *et al.* (2011) have found that the spectral AOD decreases with increase in altitude over the Himalayan range. Also, Bilal *et al.* (2013) reported that AOD has a strong relationship with elevation and high values of AOD are usually observed at lower elevations over the complex and hilly terrain of Hong Kong because steep mountain slopes create a blocking effect and this combined with a boundary layer height regularly lower than the mountains, traps pollutants in the lowlands. The lower altitude region DAC exhibits highest AOD (0.74 ± 0.26) than the other locations. The highest population in DAC is expected to contribute to anthropogenic aerosols associated with vehicular emission, household burning, constructions, etc., which is responsible for the observed elevated AOD level there. Instead of AGA, the AOD in DAC is followed by DHB. From the ISRO-GBP land campaign under conducted across the Brahmaputra Valley (Pathak *et al.,* 2014) it has been clearly shown that western locations which are inline with DAC (including DHB and GHY) are rich

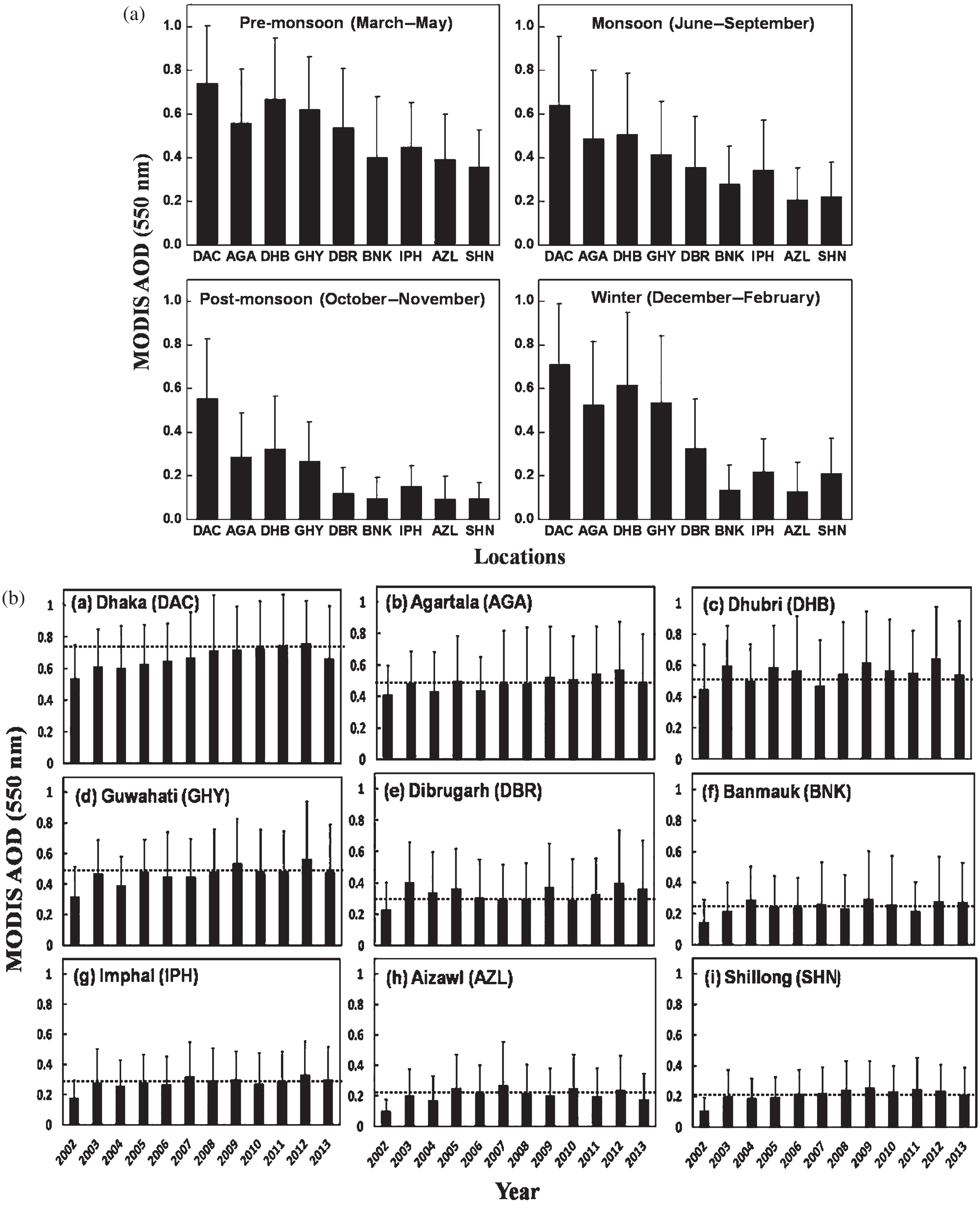

Figure 3. (a) Seasonal variation of AOD for the period July 2002–December 2013 over North-East India and adjoining areas. (b) Year to year variation of AOD averaged for the period July 2002–December 2013 over North- East India and adjoining areas. Dotted line represents climatological average AOD value.

in both particulate matter (PM) and BC concentrations as compared to eastern locations (e.g. DBR) of Brahmaputra valley which may be attributed to transportation of pollutants from highly populated and industrialized IGP region of India in addition to local pollution. Guwahati being the fastest developing metropolitan city is associated with high level of various construction activities, vehicular emissions, and these together with transportation from distant sources contributes to aerosol loading there. DBR and IPH being fast developed urban centres in the easternmost corner of India exhibit appreciable AOD next to AGA. On the other hand, in the high altitude locations AZL,

Table 1. Comparison of instantaneous CERES and SBDART flux at AOD = 0 condition

Locations	Season (2002–2013)	F_{clear} (No AOD condition)	
		SBDART Ins flux	CERES Ins flux
Dhaka (DAC) (4 m amsl)	Pre-monsoon	257.38	132.70
	Monsoon	262.54	200.50
	Post-monsoon	206.07	141.69
	Winter	200.67	132.51
Agartala (AGA) (15 m amsl)	Pre-monsoon	255.38	144.48
	Monsoon	260.81	237.98
	Post-monsoon	203.61	156.27
	Winter	198.53	139.43
Dhubri (DHB) (28 m amsl)	Pre-monsoon	256.00	165.30
	Monsoon	262.63	168.65
	Post-monsoon	200.89	144.19
	Winter	193.80	145.05
Guwahati (GHY) (55 m amsl)	Pre-monsoon	252.24	165.52
	Monsoon	259.38	168.67
	Post-monsoon	196.25	139.54
	Winter	189.76	130.70
Dibrugarh (DBR) (111 m amsl)	Pre-monsoon	243.97	151.51
	Monsoon	252.57	153.21
	Post-monsoon	185.11	141.53
	Winter	179.22	148.34
Banmauk (BNK) (279 m AMSL)	Pre-monsoon	244.55	178.08
	Monsoon	251.42	244.77
	Post-monsoon	190.32	171.98
	Winter	186.78	154.53
Imphal (IPH) (786 m AMSL)	Pre-monsoon	248.70	187.61
	Monsoon	255.39	234.84
	Post-monsoon	194.39	153.35
	Winter	189.77	133.03
Aizawl (AZL) (1001m AMSL)	Pre-monsoon	252.38	181.39
	Monsoon	258.06	262.92
	Post-monsoon	200.34	167.73
	Winter	195.94	140.78
Shillong (SHN) (1496 m AMSL)	Pre-monsoon	252.41	192.02
	Monsoon	259.19	269.43
	Post-monsoon	197.38	142.34
	Winter	191.37	132.29

BNK and SHN, low boundary layer height together with fewer urbanization results in low aerosol loading. Apart from anthropogenic aerosols, soil dust, sea salt aerosols from the Arabian Sea and BoB and biogenic aerosols from large vegetation contribute to the natural aerosols over the region.

Figure 3(b) shows the year-to-year variation of AOD for different locations in North-East India and its adjoining areas during July 2002–December 2013. For all the years of observations, the highest climatological average AOD is observed in DAC (~0.67) and the lowest is in either AZL or SHN (~0.21). The yearly averaged (2003–2013) AOD varies from its maximum value 0.68 ± 0.28 in DAC to its minimum value 0.22 ± 0.17 in SHN. The AOD values vary from the lowest value of 0.17 ± 0.16 in AZL in the year 2004 to 0.76 ± 0.27 in DAC in the year 2012. AOD attains interannual annual peak in the year 2012 at most of the locations. One of the factors controlling this is the highest fire count (MODIS-Aqua) value in that year. It is worthwhile to mention that in the interannual plot of AOD, the year 2002 has been excluded because due to unavailability of full year data. There is a slightly increasing trend in AOD over all the locations during the decade. This is consistent with the rapid growth in terms of urbanization as well as increasing population at different locations in the region. From ground-based measurements, a statistically significant increase (0.0135 per year) in column aerosol loading has also been reported over one of the present study location Dibrugarh by Babu *et al.* (2013). Kumar (2013) has also found an increasing trend (>15%) in MODIS retrieved AOD across the North Eastern part of India during the last decade (2001–2010). By using MODIS Level 2 remote sensing data, Ramachandran *et al.* (2012) have reported an increasing trend of AODs in North-East India [considering locations, e.g. Agartala (AGA), Dispur (GHY), Imphal (IPH), Aizawl (AZL) and Shillong (SHN)] and have assigned this to enhancement in the amount of aerosols produced from biomass burning and forest fires.

An intercomparison of AOD values from various satellite sensors is necessary to establish a long-term database for climatological studies and to improve the accuracy

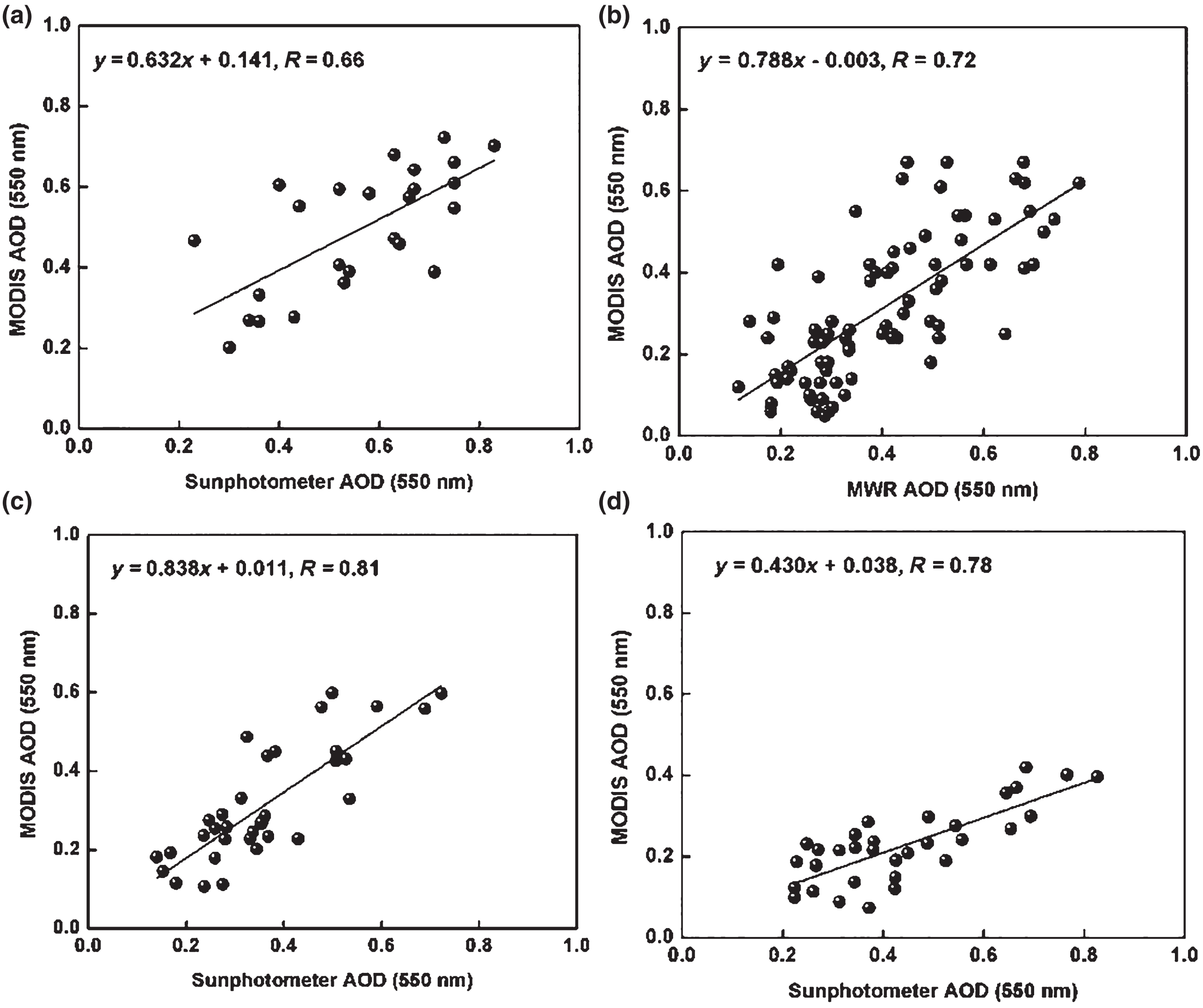

Figure 4. Scatter plot of MODIS AOD (550 nm) with Sunphotometer AOD (500 nm) for the locations: Agartala, Imphal and Shillong during September 2010–December 2013 and with MWR AOD (500 nm) in Dibrugarh during August 2002–December 2013. (a) Agartala, (b) Dibrugarh, (c) Imphal and (d) Shillong.

and coverage achievable with a single sensor (Prasad and Singh, 2007; Alam *et al.,* 2011). According to More *et al.* (2013) in order to improve the accuracy of the MODIS data, it is essential to compare and validate the MODIS data with independent ground-based measurements. Though several studies on MODIS AOD in the North-East India are now available, intercomparison of the MODIS AOD with the ground-based observations is still lacking. The relationship between MODIS AOD and ground-based AOD available at four different ARFINET stations in North-East India: AGA, DBR, IPH and SHN (Pathak *et al.,* 2016) are analysed in order to assess the accuracy of the MODIS AOD for use in this study. For the validation, the mean Microtops II Sunphotometer AOD's at 500 nm are first interpolated to a common wavelength of 550 nm of MODIS using the power law formula given by:

$$\mathrm{AOD}_{550nm} = (550/500)^{-\alpha} \times \mathrm{AOD}_{500nm} \qquad (3)$$

where α is Ångström exponent at wavelength 440–675 nm (Prasad *et al.,* 2007; Alam *et al.,* 2011) and can be determined from the spectral dependence of the measured optical depth as suggested by Ångström (1964). In DBR, AOD measurements are carried out using a Multi-Wavelength Solar Radiometer (MWR) since 2001 onwards, therefore, the correlation is examined between monthly average MODIS AOD and MWR AOD at 550 nm, the later being interpolated using Equation (3). The wavelength range of MWR for Ångström exponent in Equation (3) is 440–600 nm. At other three locations Microtops II Sunphotometer AODs are utilized (Pathak *et al.,* 2016). Both the MWR and Microtops II Sunphotometer AODs are taken at 0800 UTC corresponding to MODIS Aqua overpass time over the study region.

Figures 4(a), (c) and (d) shows the comparison of monthly averaged MODIS and Sunphotometer AOD for the period September 2010–December 2013 for the locations AGA, IPH, and SHN, respectively. The comparison between MODIS and MWR AOD over DBR for the period July 2002–December 2013 is shown in Figure 4(b). The correlation coefficient values are found

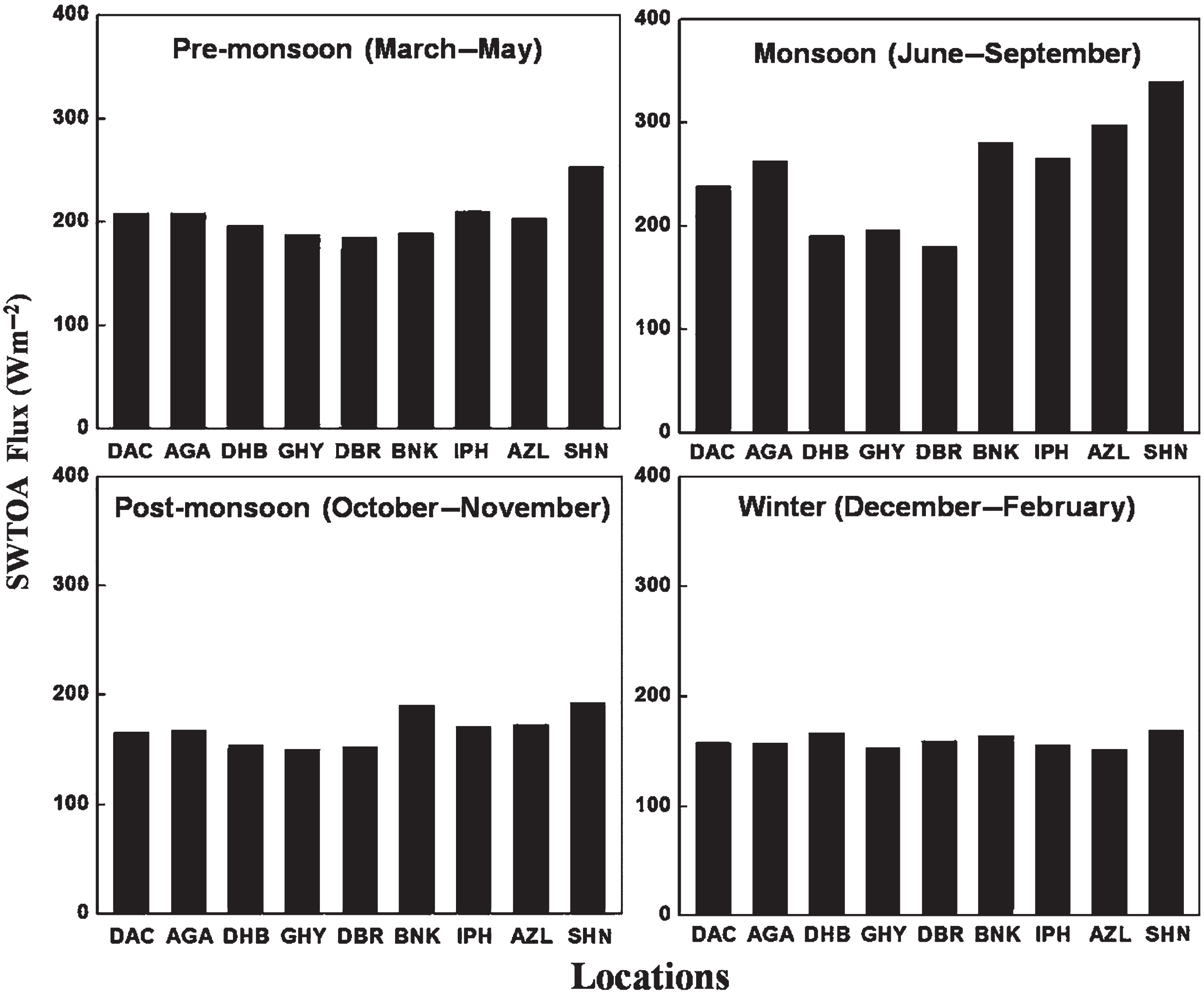

Figure 5. Seasonal variation of SW TOA Flux (with aerosol) for the period July 2002–December 2013 over North-East India and adjoining areas.

to be 0.66, 0.72, 0.81 and 0.78 over AGA, DBR, IPH, and SHN, respectively. In comparison studies, linear regression parameters, i.e. slope and intercept of the correlated plot of the collocated data is of great significance (Misra *et al.,* 2008; Levy *et al.,* 2010). The deviation of the slope of the plotted data from unity demonstrates some discrepancy in the MODIS retrievals. The measured values of slopes for the location DBR and IPH are (0.79 and 0.84, respectively) are comparatively greater than that for the locations AGA and SHN (0.63 and 0.43, respectively). Lower values (<1) of the slope for these four locations indicates an under-estimation of AOD by MODIS with respect to ground-based measurements. The non-zero intercepts of these slopes may be attributed to the biasing of the algorithm towards the low AOD values (Tripathi *et al.,* 2005; More *et al.,* 2013). The factors contributing to these imperfections may be inappropriate assumptions of surface reflectance and aerosol-type selection (Alam *et al.,* 2014). At DBR, intercept value is negative, while opposite is observed in other locations. The hilly station, SHN exhibits a very low value of the slope (<0.5) indicating the fact that the measured values of AOD are much higher than MODIS AOD. This may be due to inappropriate aerosol model in MODIS retrieval for the location. In SHN about 70% of the geographical area is covered by forest. Therefore, there is a probability of error in the retrieval of AOD by MODIS because the retrieval of AOD over forest region is less accurate than in plain vegetated area. Validation of MODIS AODs has been carried out with measurements of Chinese Sun Hazemeter NETwork (CSHNET) by many researchers (Li *et al.,* 2007; Xin *et al.,* 2007) and they have reported that AOD retrievals by MODIS are more accurate over agricultural and suburban sites than over desert (overestimate) and forests (underestimate). Satellite views a large area and hence the geophysical parameter reported is averaged over the field of view (FOV) of the satellite; but due to very narrow FOV of ground-based instruments, the measured geophysical parameter could represent only a point in the FOV of a satellite (Kumar *et al.,* 2013). This is one of the main limitations for validation of satellite retrieval products with the ground-based observations. Also, Xie *et al.* (2011) reported that the performance of the MODIS Dark Target algorithm, overall, is reliable only over moderately and highly vegetated areas. There is a need for improved space-borne aerosol remote sensing instrumentation/approaches and/or retrieval algorithms

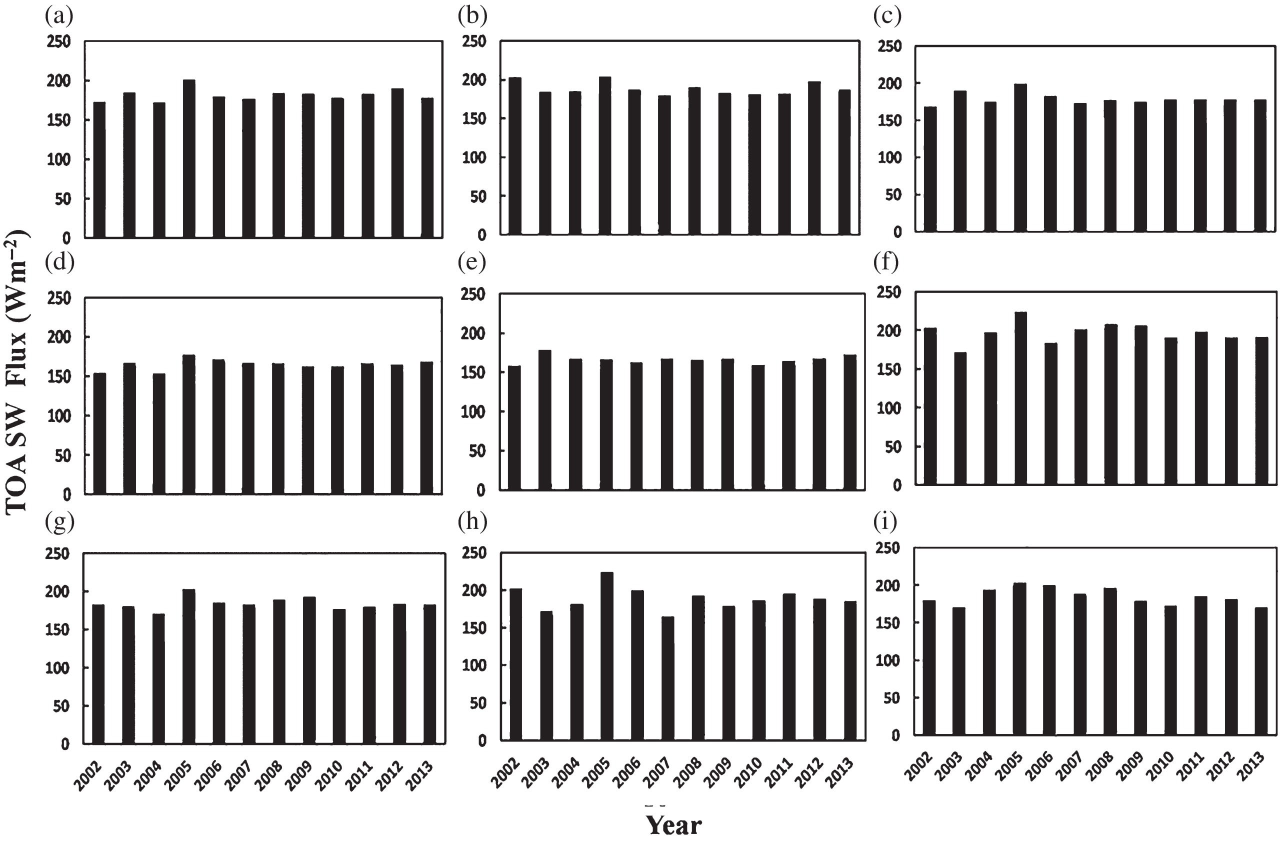

Figure 6. Year-to-year variation of TOA SW Flux for the period July 2002–December 2013 over North-East India and adjoining areas. (a) Dhaka (DAC), (b) Agartala (AGA), (c) Dhubri (DHB), (d) Guwahati (GHY), (e) Dibrugarh (DBR), (f) Banmauk (BNK), (g) Imphal (IPH), (h) Aizawl (AZL) and (i) Shillong (SHN).

for land cover types such as open shrublands and grasslands due to moderately accurate retrievals of aerosol parameters (Petrenko and Ichoku, 2013).

3.2. Spatiotemporal distribution of SWTOA flux

The methodology for determination of F_{clr} over different locations has been described in Section 2.1. Significant linear correlation is observed between MODIS-retrieved clear sky AOD at 550 nm and SW CERES TOA fluxes during the four seasons all over the region (Figure 2(b)). The seasonal mean F_{clr} in 12 years varies from the minimum value of ~131 W m^{-2} in winter over GHY to a maximum value of ~270 W m^{-2} in monsoon over SHN. For all the locations maximum SWTOA flux with no aerosol condition occurs during monsoon, whereas minimum is observed in winter except DHB and DBR where the lowest values are observed in post-monsoon.

Similar seasonal variations are exhibited by the SWTOA flux with aerosol over the nine selected locations (Figure 5). Generally, for all the locations maximum SWTOA flux is observed in monsoon and minimum in winter. DBR and DHB show slightly higher values of flux in pre-monsoon than monsoon and these locations along with GHY shows the lowest flux in post-monsoon. The magnitude of SWTOA flux varies from ~150 W m^{-2} in post-monsoon over GHY to ~340 Wm^{-2} in monsoon over SHN. It is observed that the fluxes both in presence of aerosols and in aerosol-free conditions are minimum in the locations situated across the Brahmaputra valley (DHB, GHY, DBR) while these are maximum at the high altitude locations (BNK, IPH, AZL, SHN). The maximum radiation intercepted varies according to the altitude of a location. This is because of increase in solar radiation with altitude due to the reduction of atmospheric gas molecules that absorb or scatter radiation at various wavelengths (Baker, 1978). Further for all the locations the SW flux values in aerosol-free condition are less than that with aerosol condition due to the backscattering of radiations by the aerosols into space. This reveals the cooling at TOA due to the abundance of scattering type of aerosols in the atmosphere. Similar results ($F_{\mathrm{clr}} < F_{\mathrm{aero}}$) has been observed from the diurnal variation of SW flux with aerosol and without aerosol condition in South America (Christopher and Zhang, 2002a). Further, we have compared the CERES Aqua instantaneous F_{clear} with the SBDART model derived instantaneous SW flux (at 0800 UTC) at no AOD condition (Table 1). This has been carried out only to check whether the model is capable of simulating the CERES retrieved seasonality and we have obtained a positive response at all the locations. Thus the model is further expected to provide us similar seasonality in presence of aerosols too. The CERES flux and model derived flux show good correlation. Still the observed discrepancy between these fluxes is associated

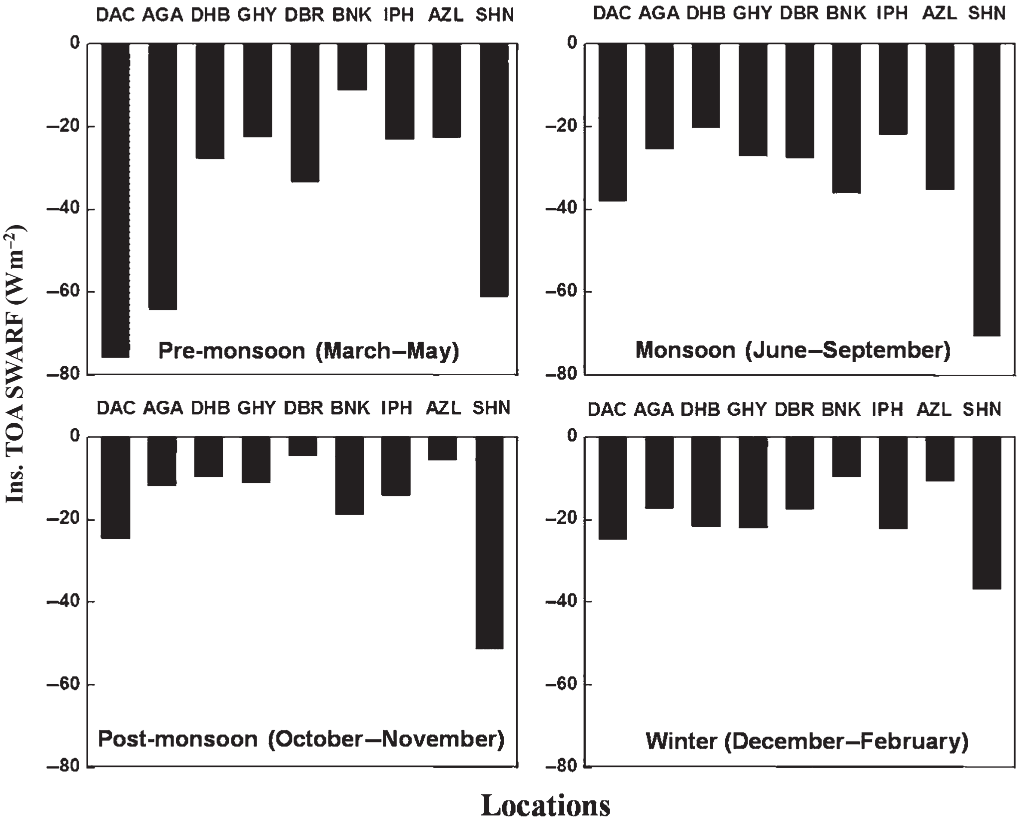

Figure 7. Seasonal variation of SW TOA Instantaneous aerosol radiative forcing for the period July 2002–December 2013 over North-East India and adjoining areas.

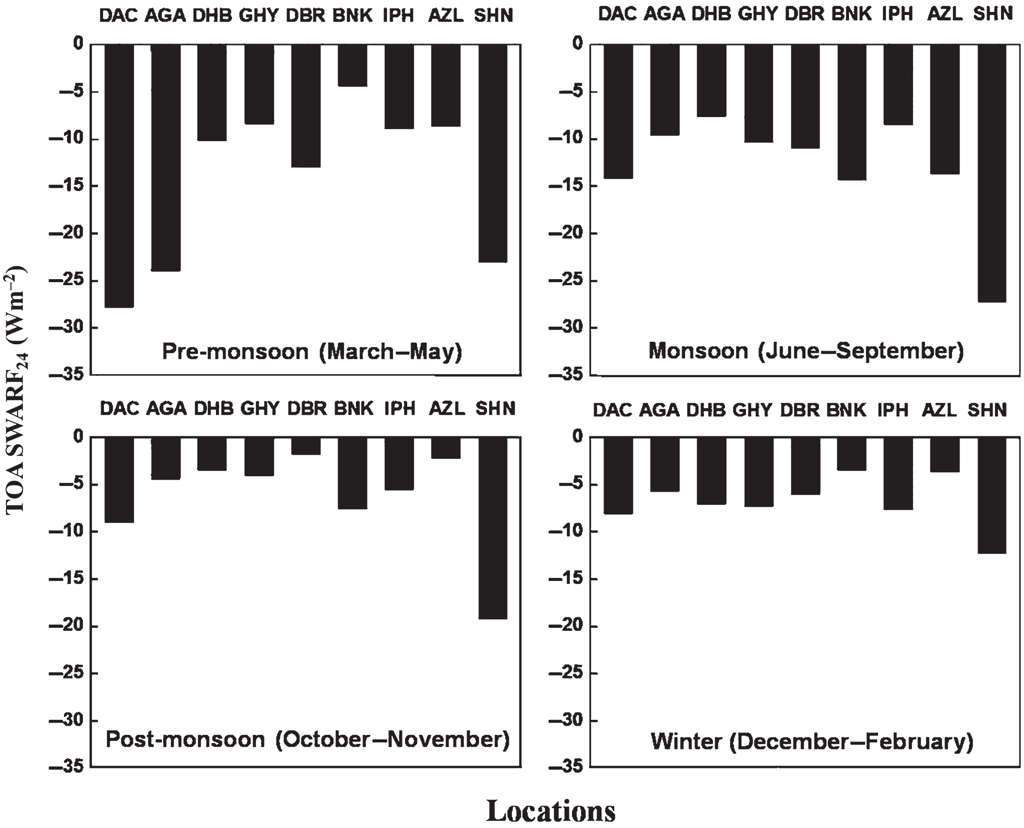

Figure 8. Seasonal variation of SW TOA diurnal average aerosol radiative forcing for the period July 2002–December 2013 over North-East India and adjoining areas.

Table 2. MODIS AOD, CERES TOA SWARF (instantaneous and diurnally averaged) and instantaneous forcing efficiency over the study region.

Location/Altitude	Season (2002–2013)	Number of data points	AOD (550 nm)	TOA instantaneous SWARF (W m^{-2})	TOA DA SWARF (W m^{-2})	Instantaneous forcing efficiency (W m^{-2} τ^{-1})
Dhaka (DAC) (4 m AMSL)	Pre-monsoon	436	0.74 ± 0.26	−75.75	−27.78	−100.46
	Monsoon	226	0.64 ± 0.31	−37.91	−14.1	−54.19
	Post-monsoon	286	0.56 ± 0.27	−24.45	−8.93	−44.87
	Winter	525	0.71 ± 0.28	−24.69	−8.02	−25.07
Agartala (AGA) (15 m AMSL)	Pre-monsoon	386	0.56 ± 0.25	−64.24	−23.86	−107.46
	Monsoon	234	0.49 ± 0.31	−25.35	−9.55	−54.93
	Post-monsoon	270	0.28 ± 0.20	−11.68	−4.33	−26.05
	Winter	544	0.52 ± 0.29	−17.07	−5.62	−37.59
Dhubri (DHB) (28 m AMSL)	Pre-monsoon	423	0.67 ± 0.28	−27.66	−10.14	−19.9
	Monsoon	249	0.51 ± 0.28	−20.16	−7.53	−52.58
	Post-monsoon	293	0.33 ± 0.24	−9.52	−3.45	−33.05
	Winter	536	0.62 ± 0.33	−21.7	−6.95	−32.76
Guwahati (GHY) (55 m AMSL)	Pre-monsoon	403	0.62 ± 0.24	−22.31	−8.34	−34.22
	Monsoon	316	0.41 ± 0.24	−26.97	−10.28	−64.57
	Post-monsoon	291	0.27 ± 0.18	−10.8	−4.01	−31.88
	Winter	521	0.54 ± 0.30	−21.92	−7.21	−35.28
Dibrugarh (DBR) (111 m AMSL)	Pre-monsoon	218	0.54 ± 0.27	−33.31	−12.95	−50.57
	Monsoon	261	0.35 ± 0.23	−27.46	−10.85	−71.65
	Post-monsoon	232	0.12 ± 0.12	−4.43	−1.74	−53.21
	Winter	450	0.33 ± 0.22	−17.33	−5.97	−45.88
Banmauk (BNK) (279 m AMSL)	Pre-monsoon	234	0.40 ± 0.28	−10.97	−4.31	−39.27
	Monsoon	168	0.28 ± 0.17	−36.03	−14.3	−181.28
	Post-monsoon	232	0.10 ± 0.10	−18.68	−7.49	−106.4
	Winter	481	0.14 ± 0.11	−9.54	−3.37	−51.96
Imphal (IPH) (786 m AMSL)	Pre-monsoon	403	0.45 ± 0.20	−22.91	−8.79	−51.96
	Monsoon	234	0.34 ± 0.23	−21.66	−8.43	−71.02
	Post-monsoon	268	0.15 ± 0.10	−13.99	−5.41	−58.62
	Winter	508	0.22 ± 0.15	−22.12	−7.58	−71.02
Aizawl (AZL) (1001 m AMSL)	Pre-monsoon	347	0.39 ± 0.20	−22.56	−8.54	−87.47
	Monsoon	212	0.21 ± 0.14	−35.22	−13.58	−199.32
	Post-monsoon	158	0.09 ± 0.10	−5.51	−2.09	−70.05
	Winter	462	0.13 ± 0.13	−10.62	−3.6	−70.81
Shillong (SHN) (1496 m AMSL)	Pre-monsoon	311	0.36 ± 0.17	−61.04	−22.99	−143.41
	Mon Monsoon	161	0.22 ± 0.16	−70.65	−27.19	−346.91
	Post-monsoon	212	0.09 ± 0.07	−51.18	−19.15	−435.97
	Winter	468	0.21 ± 0.16	−36.82	−12.22	−232.98

with model assumptions and other factors discussed in Section 2.3.

The yearly variation of TOA SW Flux (with aerosol) over each location is shown in Figure 6. In most of the years, BNK shows maximum flux with aerosol compared to other locations, while either GHY or DBR shows minimum value. In general, all the locations show a higher value of this SWTOA flux in the year 2005. Jackman *et al.* (2011) have reported that solar eruptions during the 16–21 January 2005 led to a substantial barrage of charged particles in the Earth's atmosphere which may be the cause for the highest value of SWTOA flux in the year 2005.

3.3. Spatio-temporal distribution of INSARF and DAARF

The seasonal variation of SW TOA instantaneous (INS) and diurnally averaged (DA) ARF over North-East India and adjoining areas are shown in Figures 7 and 8, respectively. The seasonal mean values of AOD and SWARF are shown in Table 2. Generally, both the INSARF and DAARF show similar seasonal variation at all the locations. The INSARF varies from −4.43 W m^{-2} in post-monsoon over DBR to −70.66 W m^{-2} in monsoon over SHN whereas the DAARF varies from −1.74 Wm^{-2} in post-monsoon season over DBR to −27.19 Wm^{-2} in monsoon over SHN. The negative TOA forcing on the average identifies aerosol scattering as the primary mechanism of radiative forcing in the region. The INSARF and DAARF are highest in pre-monsoon for the locations DAC, AGA, DHB, DBR and IPH whereas in the rest of the locations it is highest in monsoon. The minimum INSARF is generally observed in post-monsoon except for BNK and SHN where it is lowest in winter. The lowest value of CERES DAARF occurs in either post-monsoon or in winter. The pre-monsoon DAARF over the high altitude region AZL and SHN are −8.54 and −22.99 Wm^{-2}, respectively. Recently, from Aerosol Robotic Network Sun Photometer measurements over a very high altitude

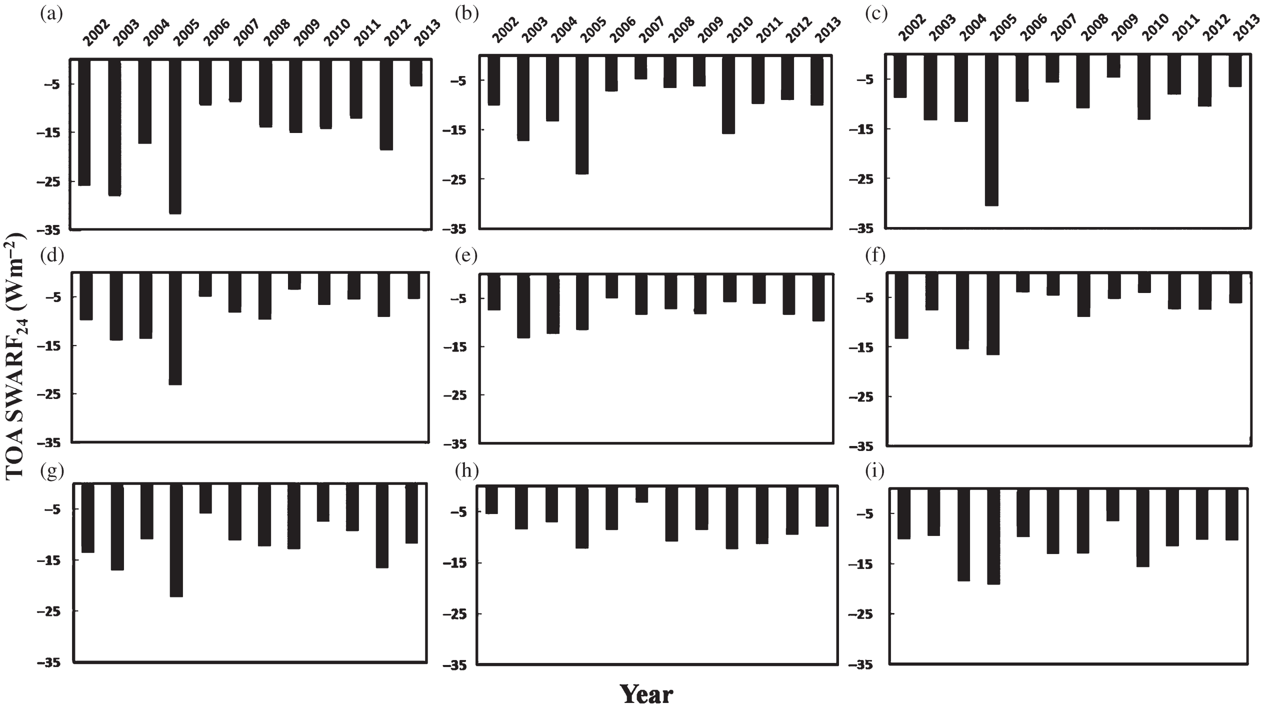

Figure 9. Year-to-year variation of diurnally averaged SWARF for the period July 2002–December 2013 over North-East India and adjoining areas. (a) Dhaka (DAC), (b) Agartala (AGA), (c) Dhubri (DHB), (d) Guwahati (GHY), (e) Dibrugarh (DBR), (f) Banmauk (BNK), (g) Imphal (IPH), (h) Aizawl (AZL) and (i) Shillong (SHN).

(1958 m AMSL) region Nainital, Dumka *et al.* (2014) have reported that the TOA, surface, and atmosphere forcing estimated to be −7.61, −45.75, and 38.14 W m^{-2}, respectively, during pre-monsoon of 2008 and 2009. Using ground-based observations, Pathak *et al.* (2010) has been reported that the magnitude of diurnally averaged ARF is highest in monsoon and lowest in the post-monsoon season over Dibrugarh for the period June 2008–May 2009. It was also reported by Pathak *et al.* (2010) that the seasonal variability of ARF over Dibrugarh might be due to variations in solar zenith angle and duration of sunshine hours over the study location. The seasonal mean TOA DAARF over the study locations ranges between −6.95 W m^{-2} in AZL and −20.39 W m^{-2} in SHN. During the pre-monsoon season, aerosols generated from biomass burning may cause an increase in aerosol forcing at the TOA. Biomass burning generates BC to organic carbon in the ratio 1:9 (Lamarque *et al.,* 2010) and thus significant scattering at the TOA may occur due to organic carbon aerosols. Generally, TOA ARF bears a good correlation with AOD and exhibits almost similar seasonal variation over the study region. Few locations (BNK, AZL and SHN) do not show one-to-one correlation between seasonal AOD and SWARF, which may be due to differences in types of aerosols, surface reflectivity, vertical aerosol distribution as well as meteorological conditions.

The intraannual variation of SW TOA DAARF shown in Figure 9 is similar to the yearly variation of SWTOA flux. The DAARF is higher in the year 2005 than the other years of observation except over DBR. In DAC higher values of DAARF are observed in the year 2002 and 2003. For all the years of observation, in general, higher values of DAARF occurs in DAC than the other locations which again is associated with the higher value of AOD. Sena *et al.* (2013) also reported that for high aerosol loading (AOD > 1 at 550 nm) the maximum daily TOA direct ARF may be as high as −20 W m^{-2} locally over Amazonia region. Patadia *et al.* (2008b) reported that over 5 years (2000–2005), TOA diurnally averaged SWARF from the CERES scanner varies between −5.2 and −9.4 W m^{-2} with a mean value of −7.6 W m^{-2} over Amazonia. They have estimated a global mean clear-sky direct radiative effect (DRE) of −5.1 ± 1.1 W m^{-2} with mean MISR AOT value of 0.18 over land. The instantaneous and 24 h mean TOA direct radiative forcing of aerosols during the biomass burning season (August–September) for the 10-year period from the year 2000 to 2009 were found to be −10.7 ± 3.3 and −5.6 ± 1.7 W m^{-2}, respectively, over Amazonia (Sena *et al.,* 2013). In South America, Christopher and Zhang (2002a) reported that the SWARF changes from −40 to −49 W m^{-2} with an average value of −45.8 ± 18.8 Wm^{-2}.

There is a possible error in estimation of DAARF by using Equation (2) which is used to expand the instantaneous aerosol forcing to a 24-h average by assuming that the aerosol loading for a particular location is constant throughout the day (Sena *et al.,* 2013). But in general, there is a considerable diurnal variation of AOD values and other parameters like water vapour, ozone concentration, etc over a location. In the SBDART model, tropical atmospheric profile is considered for all the locations with constant values of ozone, water vapour etc. However Arola *et al.* (2013) reported that the uncertainties

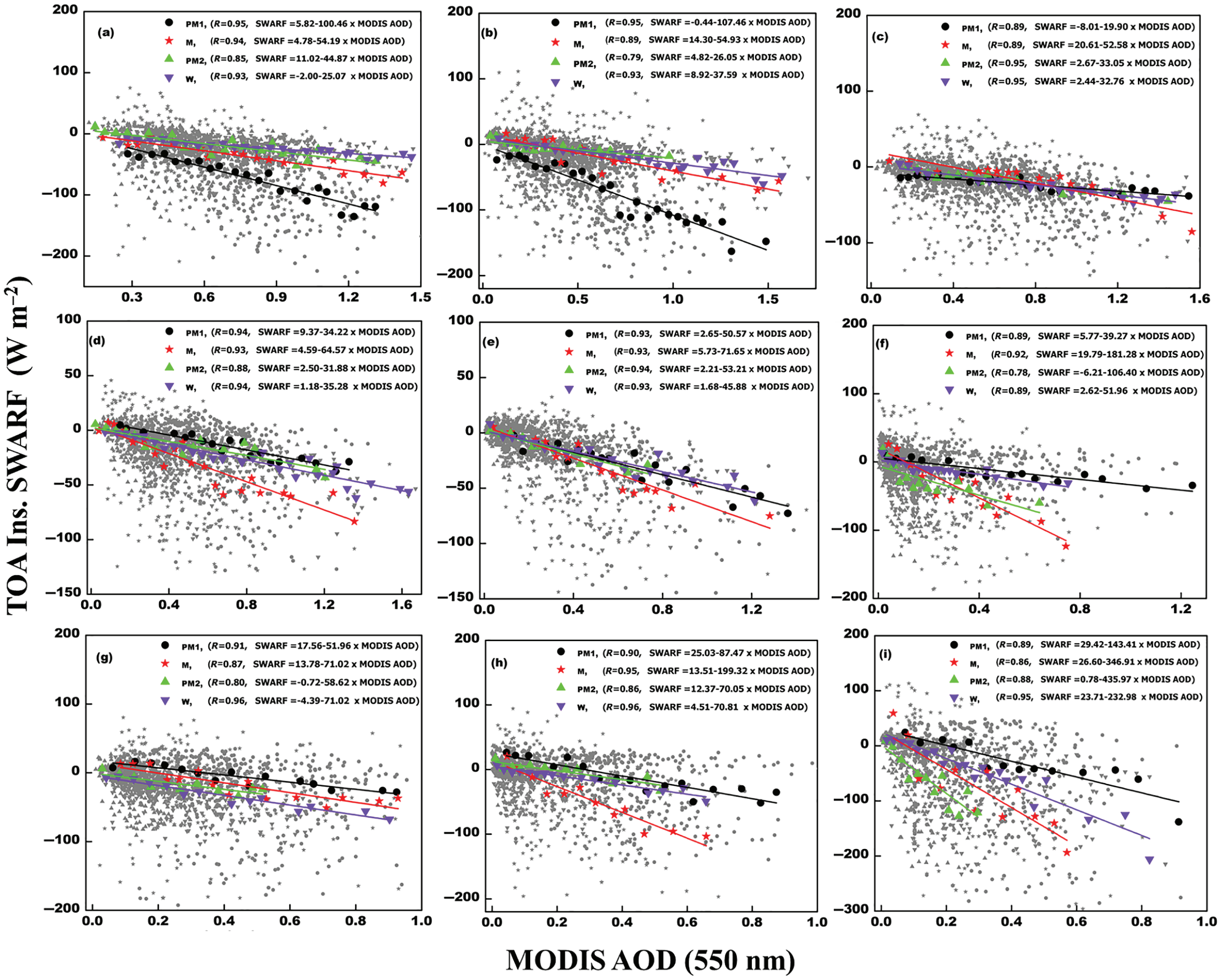

Figure 10. Methodology for seasonal instantaneous forcing efficiency calculation by using median values for the period July 2002–December 2013 over North-East India and adjoining areas (Small gray star symbol represents the instantaneous SWARF values whereas large coloured dots on each panel correspond to the median values). Different colored dots represent seasonal values (Blue = MAM, Red = JJAS, Green = ON, and Pink = DJF). The linear regression line between instantaneous ARF and AOD for all data points is also shown. (a) Dhaka, (b) Agartala, (c) Dhubri, (d) Guwahati, (e) Dibrugarh, (f) Banmauk, (g) Imphal, (h) Aizawl and (i) Shillong.

related to the diurnal variation of AOD and water vapour maybe smaller than the other uncertainties associated with the satellite-based method, therefore, the assumption of constant AOD and water vapour content is expected to have a negligible effect on radiative forcing calculations. Halthore *et al.* (1998) have shown that radiative transfer models always overestimate surface diffuse downward irradiance in a cloud-free atmosphere by 9–40%, while correctly calculating direct normal solar irradiance. From the ground-based observations over Bangalore, Satheesh *et al.* (2010) reported that the presence of elevated aerosol layers, as well as an improper description of aerosol mixing state were responsible for the discrepancies between measured and modelled-derived ARF.

3.4. Spatiotemporal distribution of instantaneous and diurnally averaged forcing efficiency

Another parameter that explains the radiative effect is the ARF efficiency which represents the efficiency of aerosols in perturbing the SW radiation. The methodology to determine the seasonal instantaneous forcing efficiency by using median values over the study locations for the period July 2002–December 2013 is shown in Figure 10. The instantaneous forcing efficiency estimation from the slope of the best-fit line between instantaneous SWARF *versus* the corresponding AOD may be affected by outliers so here we have used the median values to develop the regressions. The seasonal variation of TOA instantaneous forcing efficiency is shown in Figure 11(a), which is highest in monsoon at all the locations except over DAC and AGA, where highest is observed in pre-monsoon. SHN exhibits the maximum value of instantaneous forcing efficiency in all the seasons due to very small values of MODIS AOD and large TOA SW flux. The seasonal mean instantaneous forcing efficiency varies from its lowest value -34.49 W m^{-2} τ^{-1} over DHB to its highest value -289.82 W m^{-2} τ^{-1} in SHN (Table 2). According to Sena *et al.* (2013), the forcing

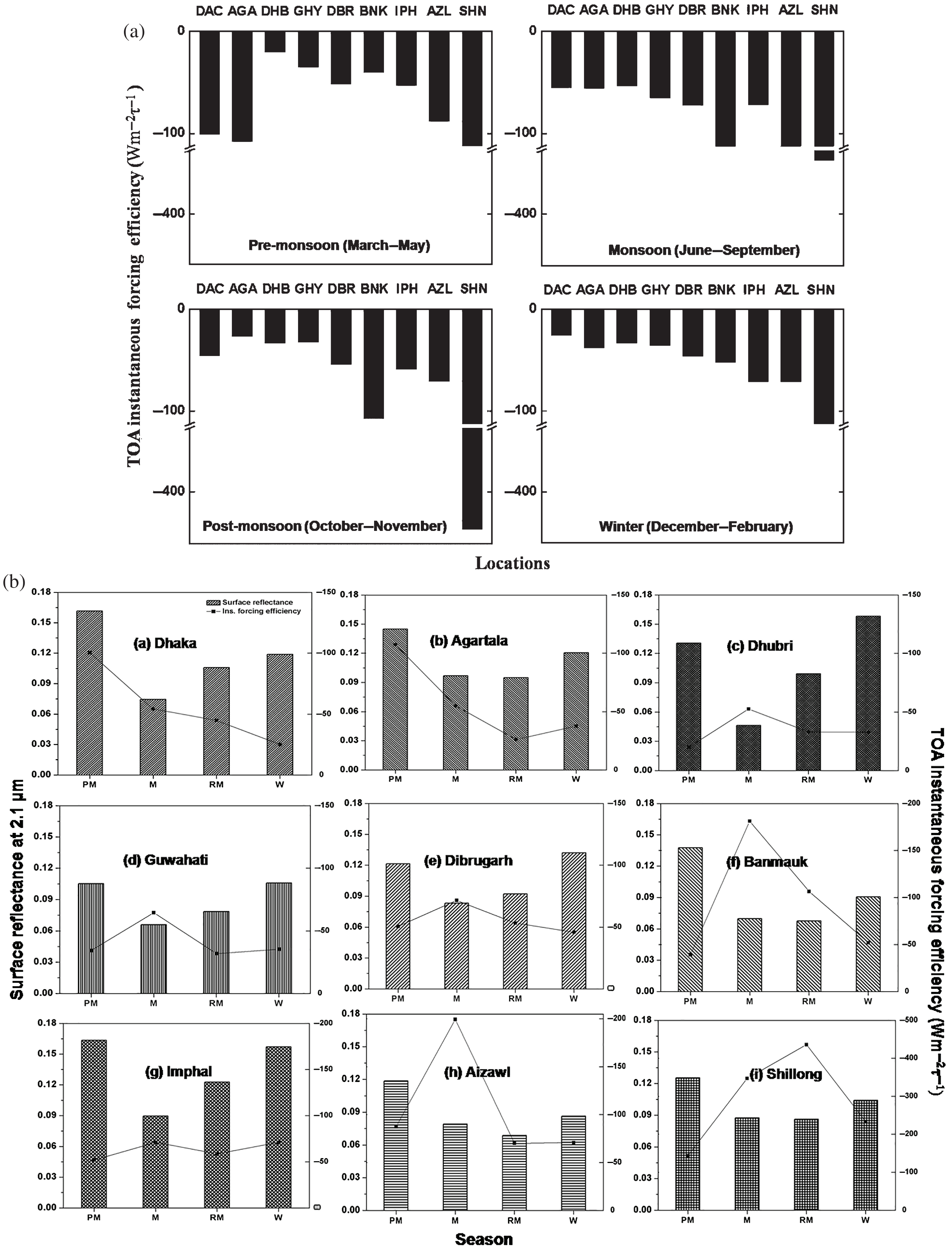

Figure 11. (a) Seasonal variation of TOA instantaneous forcing efficiency for the period July 2002–December 2013 over North-East India and adjoining areas. (b) Seasonal variation of TOA instantaneous forcing efficiency with surface reflectance at 2.1 μm for the period July 2002–December 2013 over North-East India and adjoining areas. Here PM represents pre-monsoon (March–May), M represents monsoon (June–September), RM represents post-monsoon/retreating monsoon (October–November) and W represents winter (December–February) season.

Table 3. Comparison of regional averaged AOD, instantaneous SWARF, diurnally averaged SWARF and forcing efficiency from the present study and other reports.

Locations	Year of observation	Data	AOD	SWARF$_{\text{Ins.}}$ (W m^{-2})	SWARF$_{\text{24hr avg}}$ (W m^{-2})	Forcing efficiency$_{\text{24hr avg}}$ (W m$^{-2}\tau^{-1}$)	Reference
Dhaka	July 2002–December 2013	MODIS/CERES (Aqua)	$0.67 \pm 0.28_{550\ \text{nm}}$	−43.73	−16.51	−24.68 per $\tau_{550\ \text{nm}}$	Present study
Agartala			$0.48 \pm 0.28_{550\ \text{nm}}$	−28.18	−10.8	−22.20 per $\tau_{550\ \text{nm}}$	
Dhubri			$0.55 \pm 0.30_{550\ \text{nm}}$	−28.61	−10.88	−19.72 per $\tau_{550\ \text{nm}}$	
Guwahati			$0.46 \pm 0.26_{550\ \text{nm}}$	−23.44	−9.08	−19.60 per $\tau_{550\ \text{nm}}$	
Dibrugarh			$0.33 \pm 0.25_{550\ \text{nm}}$	−20.54	−8.29	−25.10 per $\tau_{550\ \text{nm}}$	
Banmauk			$0.24 \pm 0.23_{550\ \text{nm}}$	−19.87	−8.05	- 32.82/$\tau_{550\ \text{nm}}$	
Imphal			$0.28 \pm 0.20_{550\ \text{nm}}$	−30.81	−12.22	−43.70 per $\tau_{550\ \text{nm}}$	
Aizawl			$0.21 \pm 0.19_{550\ \text{nm}}$	−21.55	−8.46	−40.73 per $\tau_{550\ \text{nm}}$	
Shillong			$0.21 \pm 0.16_{550\ \text{nm}}$	−30.34	−11.87	−56.72 per $\tau_{550\ \text{nm}}$	
Kaashidhoo	January–March 1998 and 1999	TRMM-CERES	$0.41_{500\ \text{nm}}$	–	−10	−25 per $\tau_{500\ \text{nm}}$	Satheesh and Ramanathan (2000)
Mexico	January-August 1998 and March 2000	VIRS/TRMM-CERES	$1.0_{630\ \text{nm}}$	–	−32	−32/$\tau_{630\ \text{nm}}$	Loeb and Kato (2002)
South Africa	September 2000	MODIS/CERES (Terra)	$0.14_{550\ \text{nm}}$	–	−12.7	−45/$\tau_{550\ \text{nm}}$	Christopher and Zhang (2002b)
Amazon Basin	August–September 2000–2006	MISR/CERES (Terra)	$0.24_{558\ \text{nm}}$	–	−7.6	−44.2/$\tau_{550\ \text{nm}}$	Patadia *et al.* (2008b)
South America	August 1998	VIRS/TRMM-CERES	$0.62\text{-}1.51_{640\ \text{nm}}$	−32 to −55	–	−28 to −71/ $\tau_{640\ \text{nm}}$ (Instantaneous)	Li *et al.* (2000)
Amazonia	August and September 2000–2009	MODIS/CERES (Terra)	$0.25 \pm 0.11_{550\ \text{nm}}$	−10.7 ± 3.3	−5.6 ± 1.7	(−13.1 ± 1.6)/$\tau_{550\ \text{nm}}$	Sena *et al.* (2013)
Southeast Asia	2001–2010	MODIS/CERES	$0.24 \pm 0.04_{550\ \text{nm}}$	−12.8 ± 2.1	−5.6 ± 0.8	(−20.6 ± 2.4)/ $\tau_{550\ \text{nm}}$	Feng and Christopher (2014)
China	March–October 2009	MODIS/CERES (Terra)	–	−8.8	−5.1	–	Sundström *et al.* (2015)

efficiency is higher in the forest than in savannah-like vegetation area.

A comparative assessment of observed AOD, instantaneous SWARF, diurnally averaged SWARF and diurnally averaged forcing efficiency from this study with other locations in the world have been made and presented as shown in Table 3. Diurnal averaged forcing efficiency has been calculated from the diurnally averaged SWARF divided by AOD at 550 nm. It varies from $-19.60\ \mathrm{W\,m^{-2}}$ per $\tau_{550\ \mathrm{nm}}$ in GHY to $-56.72\ \mathrm{W\,m^{-2}}$ per $\tau_{550\ \mathrm{nm}}$ over SHN. Higher altitude locations (i.e. AZL, SHN) exhibit higher values of forcing efficiency than the other locations due to their lower value of AOD. From the ground-based observations during a field campaign over a high altitude (1950 m AMSL) location, Manora Peak in Central Himalayas, Pant *et al.* (2006) have reported quite large value of forcing efficiency ($\sim$88 $\mathrm{W\,m^{-2}}$) under very low AOD and was attributed to the high value of the BC mass fraction. The estimated mean diurnally averaged TOA ARF efficiency over Amazonia is -44.2 $\mathrm{W\,m^{-2}\,\tau^{-1}}$ (Patadia *et al.,* 2008b). The mean daily TOA ARF efficiency over forest and cerrado (high surface albedo regions) regions of Amazonia is $-15.7 \pm 2.4\ \mathrm{Wm^{-2}}$ per $\tau_{550\mathrm{nm}}$ and $-9.3 \pm 1.7\ \mathrm{Wm^{-2}}$ per $\tau_{550\mathrm{nm}}$, respectively, whereas the 24-h average aerosol forcing efficiency over Amazon Basin is $-13.1 \pm 1.6\ \mathrm{W\,m^{-2}}$ per $\tau_{550\ \mathrm{nm}}$ (Sena *et al.,* 2013). Li *et al.* (2000) reported that the ratios of instantaneous TOA SWARFs per unit aerosol optical thickness at 640 nm range from −28 to −71 $\mathrm{W\,m^{-2}}$ over South America. Over the same region a mean value of forcing efficiency of $-64.6\ \mathrm{Wm^{-2}}$ per $\tau_{670\mathrm{nm}}$ has been reported by Christopher and Zhang (2002a) for the year 1998. TOA forcing as well as forcing efficiency are the functions of column AOD, vertical distribution of aerosols, type of aerosol, surface reflectance etc. Apart from looking into contribution of aerosols to TOA forcing as well as forcing efficiency we have studied the variation of forcing efficiency with surface reflectance as it plays a major role in the estimation of aerosol DRE (Sena *et al.,* 2013) and hence in forcing efficiency. The seasonal variation of TOA instantaneous forcing efficiency with surface reflectance at 2.1 μm is shown in Figure 11(b). In general, the radiative forcing efficiency becomes less negative if the surface reflectance increases for almost all the locations except DAC and AGA. There is a steep decrease in the TOA instantaneous SWARF with AOD, giving high values of slope (Figure 10) at DAC and AGA, indicating the effect of aerosols on SWARF. As the AOD is more at these two places compared to the rest of the locations (being situated in the extended IGP) that are influenced by anthropogenic emissions from IGP and local sources. Thus, it is probable that aerosol contribution to ARF and hence to forcing efficiency is dominating over surface reflectance.

4. Summary and conclusions

Twelve years of TOA CERES SW fluxes and MODIS AOD at 550 nm were analysed to assess the spatiotemporal distribution of aerosol optical and radiative properties in North-East India and adjoining areas. The following conclusions have been drawn.

1. In the North-East India and adjoining areas, the maximum aerosol loading occurs in the pre-monsoon season, whereas minimum in post-monsoon season. During the study period, the seasonal mean MODIS AOD varies from maximum value 0.67 ± 0.28 over DAC to the minimum value 0.21 ± 0.16 over AZL. The regional AOD shows a strong gradient with altitude for all the seasons. A slight increase in AOD trend is observed over the region.
2. MODIS-retrieved clear sky AOD at 550 nm and SW CERES TOA fluxes show significant linear correlation. SWTOA flux is maximum in monsoon and minimum in winter.
3. A good correlation has been observed between MODIS AOD with ground-based measured AOD for the location AGA, DBR, and IPH except over a high altitude hilly region SHN. Lower values ($<$ 1) of the slope for these four locations indicates an under-estimation of AOD by MODIS with respect to ground-based measurements.
4. Instantaneous and diurnal averages of ARF (INSARF and DAARF respectively) are highest in pre-monsoon in DAC, AGA, DHB, DBR and IPH. For the rest of the locations INSARF and DAARF are highest in monsoon season. The INSARF varies from −4.43 $\mathrm{W\,m^{-2}}$ in post-monsoon over DBR to −70.66 $\mathrm{W\,m^{-2}}$ in monsoon over SHN, whereas the DAARF varies from −1.74 $\mathrm{W\ m^{-2}}$ in post-monsoon over DBR to −27.19 $\mathrm{W\,m^{-2}}$ in monsoon over SHN.
5. The seasonal forcing efficiency is higher in monsoon over all locations except DAC and AGA, where it is highest in pre-monsoon season. The high altitude station SHN shows maximum values of instantaneous forcing efficiency in all the four seasons. In general, the radiative forcing efficiency becomes less negative if the surface reflectance increases for almost all the locations except Dhaka and Agartala.

Acknowledgements

This work has been carried out as a part of FAST TRACK Project provided to B. Pathak by Department of Science and Technology, Govt. of India, ID No. SR/FTP/ES-1/2012. The CERES-SSF and MODIS AOD data were obtained from the Atmospheric Sciences Data Center at the National Aeronautics and Space Administration (NASA)'s Langley Research Center.

References

Alam K, Qureshi S, Blaschke T. 2011. Monitoring spatio-temporal aerosol patterns over Pakistan based on MODIS, TOMS and MISR satellite data and a HYSPLIT model. *Atmos. Environ.* **45**: 4641–4651.

Alam K, Sahar NU, Iqbal Y. 2014. Aerosol characteristics and radiative forcing during pre-monsoon and post-monsoon seasons in an urban environment. *Aerosol Air Qual. Res.* **14**: 99–107, doi: 10.4209/aaqr.2013.05.0154.

Ångström A. 1964. The parameters of atmospheric turbidity. *Tellus* **16**: 64–75.

Arola A, Eck TF, Huttunen J, Lehtinen KEJ, Lindfors AV, Myhre G, Smirnov A, Tripathi SN, Yu H. 2013. Influence of observed diurnal cycles of aerosol optical depth on aerosol direct radiative effect. *Atmos. Chem. Phys.* **13**: 7895–7901, doi: 10.5194/acp-13-7895-2013.

Babu SS, Manoj MR, Moorthy KK, Gogoi MM, Nair VS, Kompalli SK, Satheesh SK, Niranjan K, Ramagopal K, Bhuyan PK, Singh D. 2013. Trends in aerosol optical depth over Indian region: potential causes and impact indicators. *J. Geophys. Res.* **118**: 1–13, doi: 10.1002/2013JD020507.

Baker PT. 1978. *The Biology of High-Altitude Peoples*. Cambridge University Press: Cambridge, 357 pp.

Bilal M, Nichol JE, Bleiweiss MP, Dubois D. 2013. A Simplified high resolution MODIS aerosol retrieval algorithm (SARA) for use over mixed surfaces. *Remote Sens. Environ.* **136**: 135–145.

Christopher SA, Zhang J. 2002a. Daytime variation of shortwave direct radiative forcing of biomass burning aerosols from GOES-8 Imager. *J. Atmos. Sci.* **59**: 681–691.

Christopher SA, Zhang J. 2002b. Shortwave aerosol radiative forcing from MODIS and CERES observations over the oceans. *Geophys. Res. Lett.* **29**: 1859, doi: 10.1029/2002GL014803.

Christopher SA, Zhang J, Kaufman YJ, Remer LA. 2006. Satellite-based assessment of top of atmosphere anthropogenic aerosol radiative forcing over cloud-free oceans. *Geophys. Res. Lett.* **33**: L15816, doi: 10.1029/2005GL025535.

Corbett JG, Su W, Loeb NG. 2012. Observed effects of sastrugi on CERES top-of-atmosphere clear-sky reflected shortwave flux over Antarctica. *J. Geophys. Res.* **117**: D18104, doi: 10.1029/2012JD017529.

Dumka UC, Moorthy KK, Tripathi SN, Hegde P, Sagar R. 2011. Altitude variation of aerosol properties over the Himalayan range inferred from spatial measurements. *J. Atmos. Sol. Terr. Phys.* **73**: 1747–1761.

Dumka UC, Tripathi SN, Misra A, Giles DM, Eck TF, Sagar R, Holben BN. 2014. Latitudinal variation of aerosol properties from Indo-Gangetic Plain to central Himalayan foothills during TIGERZ campaign. *J. Geophys. Res. Atmos.* **119**: 4750–4769, doi: 10.1002/2013JD021040.

Feng N, Christopher SA. 2013. Satellite and surface-based remote sensing of Southeast Asian aerosols and their radiative effects. *Atmos. Res.* **122**: 544–554.

Feng N, Christopher SA. 2014. Clear sky direct radiative effects of aerosols over Southeast Asia based on satellite observations and radiative transfer calculations. *Remote Sens. Environ.* **152**: 333–344.

Gogoi MM, Moorthy KK, Babu SS, Bhuyan PK. 2009. Climatology of columnar aerosol properties and the influence of synoptic conditions: first-time results from the northeastern region of India. *J. Geophys. Res. Atmos.* **114**: D08202.

Gogoi MM, Pathak B, Moorthy KK, Bhuyan PK, Babu SS, Bhuyan K, Kalita G. 2011. Multi-year investigations of near surface and columnar aerosols over Dibrugarh, north-eastern location of India: heterogeneity in source impacts. *Atmos. Environ.* **45**: 1714–1724.

Gupta P, Patadia F, Christopher SA. 2008. Multi-sensor data product fusion for aerosol research. *Geosci. Remote Sens.* **46**: 1407–1415.

Halthore RN, Nomesure S, Schuartz SE, Imre DG, Berk A. 1998. Models overestimate clear-sky surface irradiance: a case for excess atmospheric absorption. *Geophys. Res. Lett.* **25**: 3591–3594.

Hansen J, Sato M, Ruedy R. 1997. Radiative forcing and climate response. *J. Geophys. Res.* **102**: 6831–6864.

IPCC. 2007. *Climate Change 2007 - The Physical Science Basis: Working Group I Contribution to the Fourth Assessment Report of the IPCC, Climate Change 2007*. Cambridge University Press: Cambridge, UK and New York, NY.

IPCC. 2013. *Climate Change 2013 – The Physical Science Basis: Working Group I Contribution to the Fifth Assessment Report of the IPCC, Climate Change 2013*. Cambridge University Press: Cambridge, UK and New York, NY.

Jackman CH, Marsh DR, Vitt FM, Roble RG, Randall CE, Bernath PF, Funke B, Lopez-Puertas M, Versick S, Stiller GP, Tylka AJ, Fleming EL. 2011. Northern Hemisphere atmospheric influence of the solar proton events and ground level enhancement in January 2005. *Atmos. Chem. Phys.* **11**: 6153–6166.

Kalita G, Bhuyan PK. 2011. Spatial heterogeneity in tropospheric ozone over the Indian subcontinent: long-term climatology and possible association with natural and anthropogenic activities. *Adv. Meteorol.* **2011**: 924516, doi: 10.1155/2011/924516.

Keil A, Haywood JM. 2003. Solar radiative forcing by biomass burning aerosol particles during SAFARI 2000: a case study based on measured aerosol and cloud properties. *J. Geophys. Res.* **108**: 8467.

Kharol KS, Badarinath KVS, Roy PS. 2008. Studies on emission from forest fires using multi-satellite datasets over north east region of India. The International Archives of the Photogrammetry. *Remote Sens. Spatial Inf. Sci.* **37**: 473–478.

Kumar A. 2013. Variability of aerosol optical depth and cloud parameters over North Eastern regions of India retrieved from MODIS satellite data. *J. Atmos. Sol. Terr. Phys.* **100**: 34–49.

Kumar TK, Gadhavi H, Jayaraman A, Sai Suman MN, Rao SVB. 2013. Temporal and spatial variability of aerosol optical depth over South India as inferred from MODIS. *J. Atmos. Sol. Terr. Phys.* **94**: 71–80.

Lamarque JF, Bond TC, Eyring V, Granier C, Heil A, Klimont Z, Lee D, Liousse C, Mieville A, Owen B, Schultz MG, Shindell D, Smith SJ, Stehfest E, Van Aardenne J, Cooper OR, Kainuma M, Mahowald N, McConnell JR, Naik V, Riahi K, van Vuuren DP. 2010. Historical (1850–2000) gridded anthropogenic and biomass burning emissions of reactive gases and aerosols: methodology and application. *Atmos. Chem. Phys.* **10**: 7017–7039, doi: 10.5194/acp-10-7017-2010.

Levy RC, Remer LA, Kleidman RG, Mattoo S, Ichoku C, Kahn R, Eck TF. 2010. Global evaluation of the collection 5 MODIS dark-target aerosol products over land. *Atmos. Chem. Phys.* **10**: 10399–10420.

Li X, Christopher SA, Chou J, Welch RM. 2000. Estimation of shortwave direct radiative forcing of biomass-burning aerosols using new angular models. *J. Appl. Meteorol.* **39**: 2278–2291.

Li Z, Niu F, Lee K, Xin J. 2007. Validation and understanding of moderate resolution imaging spectroradiometer aerosol products (C5) using ground-based measurements from the handheld sun photometer network in China. *J. Geophys. Res.* **112**: D22S07.

Loeb NG, Kato S. 2002. Top-of-atmosphere direct radiative effect of aerosols over the tropical oceans from the Clouds and the Earth's Radiant Energy System (CERES) satellite instrument. *J. Clim.* **15**: 1474–1484.

Loeb NG, Manalo-Smith N, Kato S, Miller WF, Gupta SK, Minnis P, Wielicki BA. 2003. Angular distribution models for top-of-atmosphere radiative flux estimation from the clouds and the Earth's radiant energy system instrument on the tropical rainfall measuring mission satellite. Part I: methodology. *J. Appl. Meteorol.* **42**: 240–265.

Loeb NG, Kato S, Loukachine K, Manalo-Smith N. 2005. Angular distribution models for top-of-atmosphere radiative flux estimation from the clouds and the Earth's radiant energy system instrument on the Terra satellite. Part I: methodology. *J. Atmos. Oceanic Technol.* **22**: 338–351.

Mamun MI, Islam M, Mondol PK. 2014. The seasonal variability of aerosol optical depth over Bangladesh based on satellite data and HYSPLIT model. *Am. J. Remote Sens.* **2**: 20–29, doi: 10.11648/j.ajrs.20140204.11.

Meywerk J, Ramanathan V. 1999. Observation of the spectral clear sky aerosol forcing over the tropical Indian Ocean. *J. Geophys. Res.* **104**(24): 359–370.

Misra A, Jayaraman A, Ganguly D. 2008. Validation of MODIS derived aerosol optical depth over Western India. *J. Geophys. Res.* **113**: D04203, doi: 10.1029/2007JD 009075.

More S, Kumar PP, Gupta P, Devara PCS, Aher GR. 2013. Comparison of aerosol products retried from AERONET, MICROTOPS and MODIS over a tropical urban city, Pune, India. *Aerosol Air Qual. Res.* **13**: 107–121.

Nair VS, Babu SS, Moorthy KK. 2008. Aerosol characteristics in the marine atmospheric boundary layer over the Bay of Bengal and Arabian Sea during ICARB: spatial distribution and latitudinal and longitudinal gradients. *J. Geophys. Res. D* **113**(15): D15208.

Nakajima T, Yoon S-C, Ramanathan V, Shi G-Y, Takemura T, Higurashi A, Takamura T, Aoki K, Sohn B-J, Kim S-W, Tsuruta H, Sugimoto N, Shimizu A, Tanimoto H, Sawa Y, Lin N-H, Lee C-T, Goto D, Schutgens N. 2007. Overview of the atmospheric brown cloud east asian regional experiment 2005 and a study of the aerosol direct radiative forcing in East Asia. *J. Geophys. Res. Atmos.* **112**: D24S91, doi: 10.1029/2007JD009009.

Panicker AS, Lee D-I. 2012. A review of modeling approaches accounting for aerosol impacts on climate. In *Climate Models*, Druyan L (ed). InTech: Croatia, 249–274, ISBN: 978-953-51-0135-2.

Pant P, Hegde P, Dumka UC, Sagar R, Satheesh SK, Moorthy KK, Sah A, Srivastava MK. 2006. Aerosol characteristics at a high-altitude location in central Himalayas: optical properties and radiative forcing. *J. Geophys. Res.* **111**: D17, doi: 10.1029/2005JD006768.

Patadia F, Gupta P, Christopher SA. 2008a. First observational estimates of global clear sky shortwave aerosol direct radiative effect over land. *Geophys. Res. Lett.* **35**: L04810, doi: 10.1029/2007GL032314.

Patadia F, Gupta P, Christopher SA, Reid JS. 2008b. A multisensor satellite-based assessment of biomass burning aerosol radiative impact over Amazonia. *J. Geophys. Res.* **113**: D12214, doi: 10.1029/2007JD009486.

Pathak B, Kalita G, Bhuyan K, Bhuyan PK, Moorthy KK. 2010. Aerosol temporal characteristics and its impact on shortwave radiative forcing at a location in the northeast of India. *J. Geophys. Res.* **115**: D19204, doi: 10.1029/2009JD013462.

Pathak B, Bhuyan PK, Gogoi MM, Bhuyan K. 2012. Seasonal heterogeneity in aerosol types over Dibrugarh-North-Eastern India. *Atmos. Environ.* **47**: 307–315, doi: 10.1016/j.atmosenv.2011.10.061.

Pathak B, Bhuyan PK, Biswas J, Takemura T. 2013. Long term climatology of particulate matter and associated microphysical and optical properties over Dibrugarh, North-East India and inter-comparison with SPRINTARS simulations. *Atmos. Environ.* **69**: 334–344.

Pathak B, Borgohain A, Bhuyan PK, Kundu SS, Sudhakar S, Gogoi MM, Takemura T. 2014. Spatial heterogeneity in near surface aerosol characteristics across the Brahmaputra valley. *J. Earth Syst. Sci.* **123**: 651–663.

Pathak B, Subba T, Dahutia P, Bhuyan PK, Moorthy KK, Gogoi MM, Babu SS, Chutia L, Ajay P, Biswas J, Bharali C, Borgohain A, Dhar P, Guha A, De BK, Banik T, Chakraborty M, Kundu SS, Sudhakar S, Singh SB. 2016. Aerosol characteristics in north-east India using ARFINET spectral optical depth measurements. *Atmos. Environ.* **125**(Part B): 461–473.

Petrenko M, Ichoku C. 2013. Coherent uncertainty analysis of aerosol measurements from multiple satellite sensors. *Atmos. Chem. Phys.* **13**: 6777–6805.

Prasad AK, Singh RP. 2007. Comparison of MISR-MODIS aerosol optical depth over the Indo-Gangetic basin during the winter and summer seasons (2000-2005). *Remote Sens. Environ.* **107**: 109–119.

Prasad AK, Singh S, Chauhan SS, Srivastava MK, Singh RP, Singh S. 2007. Aerosol radiative forcing over Indo-Gangetic plains during major dust storms. *Atmos. Environ.* **41**: 6289–6301.

Rajeev K, Ramanathan V. 2001. Direct observations of clear-sky aerosol radiative forcing from space during the Indian Ocean experiment. *J. Geophys. Res.* **106**: 17221–17235.

Ramachandran S, Kedia S, Srivastava R. 2012. Aerosol optical depth trends over different regions of India. *Atmos. Environ.* **49**: 338–347.

Ramana MV, Ramanathan V, Podgorny IA, Pradhan BB, Shrestha B. 2004. The direct observations of large aerosol radiative forcing in the Himalayan region. *Geophys. Res. Lett.* **31**: L05111, doi: 10.1029/2003GL018824.

Ramanathan V, Carmichael G. 2008. Global and regional climate changes due to black carbon. *Nat. Geosci.* **1**: 221–227.

Reid JS, Hyer EJ, Johnson RS, Holben BN, Yokelson RJ, Zhang J et al. 2013. Observing and understanding the Southeast Asian aerosol system by remote sensing: an initial review and analysis for the Seven Southeast Asian Studies (7SEAS) program. *Atmos. Res.* **122**: 403–468.

Remer LA, Kaufman YJ. 2006. Aerosol direct radiative effect at the top of the atmosphere over cloud free ocean derived from four years of MODIS data. *Atmos. Chem. Phys.* **6**: 237–253, doi: 10.5194/acp-6-237-2006.

Remer LA, Kaufman YJ, Tanré D, Mattoo S, Chu DA, Martins JV, Li RR, Ichoku C, Levy RC, Kleidman RG, Eck TF, Vermote E, Holben BN. 2005. The MODIS aerosol algorithm, products and validation. *J. Atmos. Sci.* **62**: 947–973.

Ricchiazzi P, Yang S, Gautier C, Sowle D. 1998. SBDART: a research and teaching software tool for plane-parallel radiative transfer in the earth's atmosphere. *Bull. Am. Meteorol. Soc.* **79**: 2101–2114.

Salman A, Hussain T, Siddique MNA, Alam AMS. 2008. Characteristics of atmospheric trace gases, particulate matter, and heavy metal pollution in Dhaka, Bangladesh. *Air Qual. Atmos. Health* **1**: 101–109, doi: 10.1007/s11869-008-0017-8.

Satheesh SK, Ramanathan V. 2000. Large differences in tropical aerosol forcing at the top of the atmosphere and Earth's surface. *Nature* **405**: 60–63.

Satheesh SK, Vinoj VV, Moorthy KK. 2010. Radiative effects of aerosols at an urban location in southern India: observations versus model. *Atmos. Environ.* **44**: 5295–5304.

Sati VP, Rinawma P. 2014. Practices of shifting cultivation and its implications in Mizoram, North-East India: a review of existing research. *Nat. Environ.* **19**: 179–187.

Sena ET, Artaxo P. 2015. A novel methodology for large-scale daily assessment of the direct radiative forcing of smoke aerosols. *Atmos. Chem. Phys.* **15**: 5471–5483.

Sena ET, Artaxo P, Correia AL. 2013. Spatial variability of the direct radiative forcing of biomass burning aerosols and the effects of land use change in Amazonia. *Atmos. Chem. Phys.* **13**: 1261–1275.

Smith GL. 1994. Effects of time response on the point spread function of a scanning radiometer. *Appl. Opt.* **33**: 7031–7037.

Smith GL, Wielicki BA, Barkstrom BR, Lee RB, Priestley KJ, Charlock TP, Minnis P, Kratz DP, Loeb NG. 2004. Clouds and Earth Radiant Energy System (CERES): an overview. *Adv. Space Res.* **33**: 1125–1131.

Sundström A-M, Arola A, Kolmonen P, Xue Y, de Leeuw G, Kulmala M. 2015. On the use of a satellite remote-sensing-based approach for determining aerosol direct radiative effect over land: a case study over China. *Atmos. Chem. Phys.* **15**: 505–518.

Tripathi SN, Dey S, Chandel A, Srivastava S, Singh RP, Holben BN. 2005. Comparison of MODIS and AERONET derived aerosol optical depth over Ganga Basin, India. *Ann. Geophys.* **23**: 1093–1101.

Wielicki BA, Barkstrom BR, Harrison EF, Lee RB III, Smith GL, Cooper JE. 1996. Clouds and the Earth's Radiant Energy System (CERES): an earth observing system experiment. *Bull. Am. Meteorol. Soc.* **77**: 853–868.

Xie Y, Zhang Y, Xiong X, Qu JJ, Che H. 2011. Validation of MODIS aerosol optical depth product over China using CARSNET measurements. *Atmos. Environ.* **45**: 5970–5978.

Xin J, Wang Y, Li Z, Wang P, HaoWM NBL, Wang S, Liu G, Wang L, Wen T, Sun Y, Hu B. 2007. Aerosol optical depth (AOD) and Angstrom exponent of aerosols observed by the Chinese sun hazemeter network from August 2004 to September 2005. *J. Geophys. Res.* **112**: D05203.

Yan H, Huang J, Minnis P, Wang T, Bi J. 2011. Comparison of CERES surface radiation fluxes with surface observations over Loess Plateau. *Remote Sens. Environ.* **115**: 1489–1500.

Zhang J, Christopher SA. 2003. Longwave radiative forcing of dust aerosols over desert estimated from MODIS, MISR, and CERES observations from Terra. *Geophys. Res. Lett.* **30**: 2188, doi: 10.1029/2003GL018479.

Zhang J, Christopher SA, Remer LA, Kaufman YJ. 2005. Shortwave aerosol radiative forcing over cloud-free oceans from Terra: 2 Seasonal and global distributions. *J. Geophys. Res.* **110**: D10S24, doi: 10.1029/2004JD005009.